An anti-SARS-CoV-2 non-neutralizing antibody with Fc-effector function defines a new NTD epitope and delays neuroinvasion and death in K18-hACE2 mice

Guillaume Beaudoin-Bussières[1,2,14], Yaozong Chen[3,14], Irfan Ullah[4,14], Jérémie Prévost[1,2], William D. Tolbert[3], Kelly Symmes[4], Shilei Ding[1], Mehdi Benlarbi[1], Shang Yu Gong[1,5], Alexandra Tauzin[1,2], Romain Gasser[1,2], Debashree Chatterjee[1], Dani Vézina[1], Guillaume Goyette[1], Jonathan Richard[1,2], Fei Zhou[13], Leonidas Stamatatos[6,7], Andrew T. McGuire[6,7,8], Hughes Charest[9], Michel Roger[1,2,9], Edwin Pozharski[11,12], Priti Kumar[4], Walther Mothes[10], Pradeep D. Uchil[10,#], Marzena Pazgier[3,#] and Andrés Finzi[1,2,5,15,#]

[1]Centre de recherche du CHUM. Montreal, QC H2X 0A9, Canada
[2]Département de Microbiologie, Infectiologie et Immunologie, Université de Montréal, Montreal, QC H2X 0A9, Canada
[3]Infectious Disease Division, Department of Medicine, Uniformed Services University of the Health Sciences, Bethesda, MD 20814-4712, USA
[4]Department of Internal Medicine, Section of Infectious Diseases, Yale University School of Medicine, New Haven, CT 06520, USA
[5]Department of Microbiology and Immunology, McGill University, Montreal, QC H3A 2B4, Canada
[6]Vaccine and Infectious Disease Division, Fred Hutchinson Center, Seattle, WA 98195, USA
[7]Department of Global Health, University of Washington, Seattle, WA 98195, USA
[8]Department of Laboratory Medicine and Pathology, University of Washington, Seattle, WA 98195, USA
[9]Laboratoire de Santé Publique du Québec, Institut national de santé publique du Québec, Sainte-Anne-de-Bellevue, QC H9X 3R5, Canada
[10]Department of Microbial Pathogenesis, Yale University School of Medicine, New Haven, CT 06510, USA
[11]University of Maryland Institute for Bioscience and Biotechnology Research, Rockville, MD 20850, USA
[12]Department of Biochemistry and Molecular Biology, University of Maryland School of Medicine, Baltimore, MD 21201, USA
[13] Division of Basic and Translational Biophysics, Unit on Structural Biology, NICHD, NIH, Bethesda, MD, 20892, USA
[14]These authors contributed equally
[15]Lead contact

corresponding authors
Pradeep Uchil pradeep.uchil@yale.edu
Marzena Pazgier marzena.pazgier@usuhs.edu
Andrés Finzi andres.finzi@umontreal.ca

Running Title: Fc-mediated effector functions against SARS-CoV-2 infection in mice

Keywords: SARS-CoV-2, COVID-19, coronavirus, Spike glycoproteins, non-neutralizing antibodies, ADCC, K18-hACE2 mice, Fc-effector functions

Summary

Emerging evidence in animal models indicate that both neutralizing activity and Fc-mediated effector functions of neutralizing antibodies contribute to protection against SARS-CoV-2. It is unclear if antibody effector functions alone could protect against SARS-CoV-2. Here we isolated CV3-13, a non-neutralizing antibody from a convalescent individual with potent Fc-mediated effector functions that targeted the N-terminal domain (NTD) of SARS-CoV-2 Spike. The cryo-EM structure of CV3-13 in complex with SAR-CoV-2 spike revealed that the antibody bound from a distinct angle of approach to a novel NTD epitope that partially overlapped with a frequently mutated NTD supersite in SARS-CoV-2 variants. While CV3-13 did not alter the replication dynamics of SARS-CoV-2 in a K18-hACE2 transgenic mouse model, an Fc-enhanced CV3-13 significantly delayed neuroinvasion and death in prophylactic settings. Thus, we demonstrate that efficient Fc-mediated effector functions can contribute to the *in vivo* efficacy of anti-SARS-CoV-2 monoclonal antibodies in the absence of neutralization.

Introduction

In December of 2019, a new coronavirus was detected in Wuhan, China which has subsequently been named severe acute respiratory syndrome coronavirus 2 (SARS-CoV-2) (Huang et al., 2020; Wu et al., 2020b; Zhu et al., 2020). This novel virus is an enveloped, positive-strand RNA coronavirus that is a member of the β-coronavirus genus (Huang et al., 2020; Wu et al., 2020b; Zhu et al., 2020). This genus also contains SARS-CoV-1 and MERS-CoV which caused pandemics in 2002 and 2012, respectively (Ksiazek et al., 2003; Zaki et al., 2012). SARS-CoV-2, however, has caused a much larger pandemic with millions of deaths worldwide (Worldometer, 2021). The efficacy with which SARS-CoV-2 transmits between humans has led to COVID-19 being one of the largest and fastest growing pandemics in the past century. The COVID-19 pandemic has caused a massive loss of human life, extreme economic consequences and disrupted billions of human lives worldwide. For these reasons, billions of dollars have been invested in the development of vaccines against SARS-CoV-2 which has resulted in their development in record time. Several vaccine platforms have been approved in different jurisdictions worldwide to counter the COVID-19 pandemic (Oliver et al., 2021a; Oliver et al., 2021b; Polack et al., 2020; Voysey et al., 2021) with vaccine development primarily focused on generating immune responses against the SARS-CoV-2 Spike glycoprotein. The Spike glycoprotein mediates viral entry and is well exposed at the surface of virions (Duan et al., 2020; Shang et al., 2020) and infected cells (Buchrieser et al., 2020). The Spike glycoprotein is a trimer of heterodimers, composed of 2 subunits, S1 and S2, generated by furin cleavage of a single S polypeptide. The S1 subunit permits attachment via its receptor binding domain (RBD) to the cellular receptor angiotensin

converting enzyme 2 (ACE2) (Hoffmann et al., 2020; Lan et al., 2020; Walls et al., 2020; Wrapp et al., 2020b). It also contains an N-terminal domain (NTD) that may aid attachment and conformational transition of Spike, as previously observed for other coronaviruses. (Amraie et al., 2020; Lempp et al., 2021; Soh et al., 2020). Once bound to ACE2, a series of conformational changes allows the S2 subunit to mediate fusion between the cellular and viral membranes. Virus neutralization has been shown to be important for controlling SARS-CoV-2 infection in vaccinated human cohorts (AstraZeneca and Iqvia Pty, 2021; Bio and Pfizer, 2021; Janssen and Prevention, 2021; ModernaTx et al., 2022). As a result, considerable effort has been made to study antibody-mediated neutralization and its effect in mitigating SARS-CoV-2 infection. Many neutralizing antibodies target the RBD, but some targeting the NTD and the S2 subunits have also been described (Cao et al., 2020; Chen et al., 2020; Chi et al., 2020; Jennewein et al., 2021; Ju et al., 2020; Li et al., 2021b; Liu et al., 2020; Rappazzo et al., 2021; Seydoux et al., 2020; Suryadevara et al., 2021; Ullah et al., 2021; Voss et al., 2021; Wang et al., 2020; Wrapp et al., 2020a; Wu et al., 2020c; Yuan et al., 2020). However, some studies have shown that around 25% to 45% of people who resolve the infection have plasma with low or undetectable levels of SARS-CoV-2 neutralizing activity (Beaudoin-Bussieres et al., 2020; Luchsinger et al., 2020; Muecksch et al., 2021; Payne et al., 2020; Prevost et al., 2020; Robbiani et al., 2020; Wu et al., 2020a). These data suggest that immune functions other than neutralization could play a role in SARS-CoV-2 control. Accordingly, results from a phase III clinical trials show a vaccine efficacy of >90% starting 14 days after the injection of a single dose of a BNT162b2 mRNA vaccine, a time at which neutralizing activity from the vaccine is weak (Baden et al., 2021; Polack

et al., 2020; Skowronski and De Serres, 2021; Tauzin et al., 2021). Similarly, recent studies have shown that despite a significant loss in neutralizing activity against the B.1.1.7 (Alpha) and B.1.351 (Beta) variants, the AstraZeneca and Pfizer/BioNTech vaccines remain efficacious against these variants (Emary et al., 2021) (Pfizer/BioNTech, 2021).

The antigen binding domain (Fab) of antibodies is critical for neutralization but the crystallizable fragment (Fc) of the antibody can contribute significantly to their *in vivo* efficacy (Bournazos et al.,2019; Bournazos et al., 2014; DiLillo et al., 2014). Fc engagement of Fc gamma receptors (FcγRs) elicits complement-dependent cytotoxicity (CDC), antibody-dependent cellular cytotoxicity (ADCC) and antibody-dependent cellular phagocytosis (ADCP) depending on the effector cell to which they bind. We previously examined the protection mediated by neutralizing antibodies (NAbs) targeting the SARS-CoV-2 Spike in a K18-hACE2 mouse model and the effect of wild-type or Fc-mutated versions of these NAbs in a prophylactic or therapeutic setting (Ullah et al., 2021). The Fc mutations (L234A-L235A, also referred to as LALA), significantly diminished the affinity of antibodies to FcγRIIIa and also impacted Fc-mediated effector functions. Interestingly, in this study we showed LALA mutations significantly diminished the capacity of NAbs to protect mice from a lethal SARS-CoV-2 challenge (Ullah et al., 2021). Similarly, two other studies examining humoral responses in acutely infected individuals found that Fc-mediated effector functions were associated with survival (Brunet-Ratnasingham et al., 2021; Zohar et al., 2020). Therefore, while

126 antibody-mediated neutralization was required for protection, it was not sufficient for
127 viral control.

128 Serological analysis of the plasma or serum from SARS-CoV-2-infected individuals from
129 multiple sources (Harvey et al., 2021; McCallum et al., 2021; Piccoli et al., 2020)
130 revealed that ~65-80% of the neutralizing response was from RBD-specific antibodies,
131 with a smaller portion targeting the NTD (~6-20%) or the S2 subunit (4-20%). Although
132 the glycan-shielded NTD has been proposed to have limited immunogenicity as
133 compared to RBD, NTD-directed antibodies are regarded as a major driving force in
134 imposing selection pressure against the virus eliciting many NTD escape mutations and
135 deletions in emerging SARS-CoV-2 variants (McCallum et al., 2021). Notably, NTD-
136 directed monoclonal NAbs whose structures have been determined recognized a similar
137 glycan-free epitope (Cerutti et al., 2021; Chi et al., 2020; Liu et al., 2020; McCallum et
138 al., 2021; Sun et al., 2021; Voss et al., 2021), named the NTD-supersite (residue 14-20,
139 140-158 and 245-264) (Harvey et al., 2021; McCallum et al., 2021). There are a greater
140 number of mutations within the NTD supersite than in the NTD scaffold that highlights
141 its importance to the virus (McCarthy et al., 2021). Given that the NTD-supersite-
142 directed NAbs do not interfere with the ACE2-RBD interaction or the shedding of the S1
143 subunit, their mechanism of neutralization is yet to be determined. Possible mechanisms
144 could include interactions with co-receptors, proteolytic activation by TMPRSS2, or
145 interference with membrane-fusion.

146 Here we sought to test if Fc-mediated effector functions of antibodies alone could
147 mediate virological control in a lethal K18-hACE2 transgenic mouse model of SARS-
148 CoV-2 using CV3-13, a non-neutralizing antibody with potent Fc-effector functions. Our

149 cryo-EM structure revealed that CV3-13 binds to a novel NTD epitope that partially
150 overlaps with the NTD supersite with a distinct angle of approach, adding to our
151 understanding of how fine epitope specificity and the mode of antibody binding can
152 contribute to antibody function. Several recurrent NTD mutations outside of the NTD
153 supersite associated with immune resistance are found within the CV3-13 epitope, e.g.
154 the N2 loop and the newly identified N2-3 hairpin, suggesting that the epitope coincides
155 with those of other NTD-binding antibodies. While administration of CV3-13 under both
156 prophylactic and therapeutic regimens did not change the replication dynamics of SARS-
157 CoV-2 in a K18-hACE2 transgenic mouse model, an Fc-enhanced version of CV3-13
158 significantly delayed neuroinvasion and death from a lethal challenge of the virus in a
159 prophylactic setting. Thus, using a NTD-binding non-neutralizing antibody, we
160 demonstrate the contribution of Fc-effector functions in mitigating viral-induced
161 pathogenesis.
162

Results

CV3-13 binds the NTD of the Spike glycoprotein

To test if non-neutralizing antibodies alone can protect from SARS-CoV-2 infection, we characterized a non-neutralizing antibody isolated from the peripheral blood mononuclear cells (PBMCs) of a convalescent individual (CV3) 6 weeks after the onset of symptoms. Using fluorescent SARS-CoV-2 Spike 2P as a probe, we sorted four hundred thirty-two antigen-specific B cells from this donor PBMCs. We successfully generated twenty-seven monoclonal antibodies and tested their ability to neutralize pseudoviral particles carrying Spike protein. CV3-13 bound to Spike but did not neutralize SARS-CoV-2 pseudovirus (Jennewein et al., 2021). To determine the epitope recognized by CV3-13, we analyzed its ability to bind different Spike variants on the surface of transfected cells. CV3-13 efficiently bound the WT (Wuhan-Hu-1 reference strain) and the D614G variant but did not recognize the Spike from the B.1.1.7 (alpha) variant (Figure 1A, B). We took advantage of this differential binding capacity to determine the epitope of CV3-13 by sequentially introducing B.1.1.7 variant mutations into the WT Spike. CV3-13 recognized all but the Δ144 mutant that had a single amino acid deletion located in the S1 NTD (Figure 1B). In agreement with our cell surface binding analyses, surface plasmon resonance (SPR) showed that CV3-13 binds to the SARS-CoV-2 S1 subunit (Figure 1C). Monovalent CV3-13 Fab bound to the stabilized Spike trimer ectodomain (Spike-6P) with nanomolar affinity (K_D = ~55 nM) (Figure 1D).

CV3-13 is a non-neutralizing antibody with potent Fc-mediated effector functions

To confirm that CV3-13 was a non-neutralizing antibody (Jennewein et al., 2021), we tested its capacity to neutralize pseudoviruses carrying the SARS-CoV-2 Spike. For comparison purposes, we used CV3-1, a potent RBD-targeting NAb, as a positive control (Jennewein et al., 2021). CV3-1 was recently shown to protect K18-hACE2 mice from a lethal SARS-CoV-2 challenge in a Fc-effector function-dependent manner (Ullah et al., 2021). Our analyses showed that CV3-13 was unable to neutralize pseudoviral particles (Figure 2A) bearing SARS-CoV-2 Spike or the live virus (Figure 2B). Introduction of LALA or GASDALIE mutations to the Fc portion of the antibody did not modify its neutralization profile (Figure 2A) or its ability to recognize the Spike whether it be at the surface of infected cells, transduced cells or the recombinant SARS-CoV-2 S-6P (Figure 2C, D, S1). The LALA (L234A/L235A) mutations impair the interaction between the IgG Fc portion and FcγRs (Saunders, 2019), while GASDALIE (G236A/S239D/A330L/I332E) mutations strengthen these interactions (Bournazos et al., 2014; DiLillo and Ravetch, 2015; Lazar et al., 2006; Richards et al., 2008; Smith et al., 2012). Having established that CV3-13 does not mediate neutralization (Figure 2A, B), we then evaluated whether it could mediate Fc-effector functions. To this end we used an antibody-dependent cellular cytotoxicity (ADCC) assay using a human T-lymphoid cell line resistant to NK cell-mediated cell lysis (CEM.NKr) and stably expressing the full-length Spike on their surface as target cells. PBMCs from healthy individuals were used as effector cells, as previously reported (Anand et al., 2021). In agreement with a previous study, CV3-1 mediated robust ADCC (Ullah et al., 2021) (Figure 2E). CV3-13 mediated ADCC to a similar level as CV3-1 (Figure 2E). Introduction of the GASDALIE

mutations enhanced CV3-13-mediated ADCC to levels surpassing those achieved with CV3-1 or CV3-13 WT at higher concentrations (Figure 2E). As expected, introduction of the LALA mutations significantly decreased CV3-13-mediated ADCC (Figure 2E). CV3-13 GASDALIE mediated similar ADCP as its WT counterpart, while CV3-13 LALA mediated reduced ADCP (at all tested concentrations) than both CV3-13 WT and CV3-13 GASDALIE (Figure 2F). Altogether, these results confirm that CV3-13 is a non-neutralizing antibody able to mediate Fc-mediated effector functions.

Structural analyses of the CV3-13 Fab and SARS-CoV-2 spike complex defines a novel NTD epitope

To define the CV3-13 epitope and gain a more comprehensive understanding of how CV3-13 triggers potent Fc-mediated cytotoxicity without directly neutralizing the SARS-CoV-2 virus, we determined the cryo-EM structure of SARS-CoV-2 HexaPro Spike in complex with CV3-13 Fab at a resolution of 4.45 Å (FSC cut-off 0.143) using C1-symmetry (Figure 3 and S4). The Spike trimer presented itself in the one-RBD-up conformation with each of the N-terminal domain (NTD) bound to one CV3-13 Fab to the furthest lateral side of the spike relative to the spike-trimer axis. Despite the asymmetric RBD conformation in the three spike protomers, the three CV3-13-NTD interfaces were identical. Global refinement imposed with C3 symmetry improved the overall resolution to 4.19 Å and permitted a detailed analysis of the CV3-13 footprint. The C3-symmetry map was therefore used in all further structural analysis (Figure 3 and S4).

The structure of CV3-13 Fab bound to SARS-CoV-2 HexaPro Spike is shown in Figure 3A. The variable heavy and light chain regions (V_H and V_L) of CV3-13 were well defined in the density. The constant part of the Fab was disordered, however, and is omitted from the model. CV3-13 binds to the NTD, at an almost right angle relative to the stem region of the spike. Both heavy and light chain complementarity determining regions (CDRs) of CV3-13 contribute almost equally to antigen recognition with CDR H3, CDR L1 and CDR L3 having the greatest number of contacts. The total buried surface area (BSA) in complex formation is 1184 $Å^2$ which is comparable to the BSA of typical complexes formed by other NTD-specific antibodies (Figure 3B). Four out of five highly mobile NTD loops as defined by Chi et al., (Chi et al., 2020), e.g.: N2 (residues 67-79), N3 (residues 141-156), N4 (residues 177-186) and N5 (residues 246-260) are stabilized by the associated CV3-13 Fab (Figure 3C). The fifth antigenic NTD loop N1 (residues 14-26) is distal from the CV3-13 binding site and exhibits a higher degree of mobility in the complex. Of the antibody CDRs, the 14-amino-acid CDR H3, consisting of 7 aromatic residues (six tyrosines and one phenylalanine), stretches into the hydrophilic groove formed by the positively charged N3 and N4 loops, the N2 and N3 loops, and the glycan-shielded Asn^{122}. CV3-13 forms extensive contact with N2, N4 and a buried N2 to N3 loop hairpin (residues 95-102) which are rarely involved in the epitopes of other known NTD-mAbs (Figure 4C). Interestingly, CV3-13 relies on key π-π interactions through its CDR H3 tyrosines to the Tyr^{144}-Tyr^{145} stretch of N3 that is frequently mutated in SARS-CoV-2 emerging variants. For example, the single residue deletion of Tyr^{144} (as first detected in the B.1.1.7 variant) which was used to initially characterize CV3-13 causes a complete abrogation of CV3-13 binding (Figure 1B).

The footprint of CV3-13 epitope differs from all known NAbs that recognize the NTD. Neutralizing NTD-directed antibodies target similar glycan-free epitopes located in the upper protruding area of the NTD, referred to as the "NTD supersite" of vulnerability (Cerutti et al., 2021; Harvey et al., 2021; McCallum et al., 2021). The non-neutralizing CV3-13 targets a distinct lateral region of the spike closer to the viral membrane surface, which only marginally overlaps with the supersite (Figure 4A). The distinct angle of approach of CV3-13 enables its extended CDR H3 to access the buried N2 to N3 hairpin which does not interact with the reported NTD-directed mAbs. Given that the NTD mutations found in escape variants of SARS-CoV-2 are thought to be the direct result of NTD-specific antibody selection, the emergence of the T95I mutation in the N2 to N3 hairpin, as first seen in the B.1.526 (Iota) and B.1.617.1 (Kappa) variants (Figure S6), suggests that this region represents a new antigenic site that can be targeted by non-neutralizing antibodies. Interestingly, the immunogenic N3 and N5 loops, which form the major interacting motifs for currently characterized NTD mAbs and is the primary component of the NTD supersite, only makes minor contact with the CDR H3, L1 and L2 of CV3-13. As a result, the backbone residues of the N3 and N5 loops are less traceable in the density map (Figure S5) and appear to adopt markedly different conformations as compared with those observed for neutralizing anti-NTD mAb structures (Figure 4E). Overall, the N3 and N5 loops which form the majority of the NTD supersite are less important for CV3-13 binding. Instead, CV3-13 utilizes the N2 and N4 loops and N2 to N3 hairpin, which are located at the lateral/bottom side of the NTD and are rarely accessed by the NTD-directed NAbs that bind from the top of the NTD. Our data are

consistent with the finding that N3 and N5 loop engagement is an important component of NTD directed antibody neutralization of SARS-CoV-2.

CV3-13 has a distinct angle of approach and induces conformational rearrangements in the NTD as compared to other NTD-binding mAbs

To gain structural insight on how the antibody recognition site and its angle of approach to the SARS-CoV-2 spike NTD affects the mode of action (i.e., potent neutralizers targeting the supersite versus non-neutralizing antibodies), we aligned the NTD-Fv portions of CV3-13 and other reported NTD-directed antibodies based on the rigid NTD core. The comparisons consisted of antigen-Fab structures for whose PDB models are available. There are in total eleven neutralizing antibodies targeting the NTD supersite as well as the other three which recognize the so-called infectivity-enhancing site (Li et al., 2021a; Liu et al., 2021; McCallum et al., 2021). As shown in Figure 4A, CV3-13 approaches the NTD at a nearly perpendicular angle relative to the spike trimer axis with its epitope footprint only partly overlapping the NTD supersite and the infectivity-enhancing site. The supersite binding antibodies access the NTD from the top of the spike trimer, while antibodies targeting the infectivity-enhancing site approach the spike from the bottom, closer to the viral membrane. The differences in binding modes of CV3-13 and other NTD-specific antibodies are evident when the angles of approach (defined as the angle between the average Cα position for the Fv of each individual mAb (Cα-Fv), and the average Cα position for the NTD as a whole (Cα-NTD), using the average Cα position of the C-terminal helix (residues 295-303) of the NTD (Cα-NTD-C-term) as the origin to exclude any differences due to the conformational state of the NTD relative to

299 the spike as a whole) are calculated (Figure 4B). The supersite-binding NAbs approach
300 the NTD with a similar angle (in a range of 6^{o} -15^{o}), substantially different from that of
301 CV3-13 with a calculated angle ~30^{o} (Figure 4B). In contrast, the infectivity-enhancing
302 antibodies use the angle of approach in the range of 45^{o}-60^{o}. Also, the fine epitope
303 specificity of CV3-13 is different with contact regions only partially overlapping with
304 neutralization supersite (Figure 4C). To summarize, CV3-13 uses the binding angle that
305 positions it somewhere between the binding angles of antibodies recognizing the
306 neutralization supersite, that bind from the top of the spike and antibodies targeting the
307 infectivity-enhancing site, that bind at the bottom of spike, closer to the viral membrane.
308 These features are likely why CV3-13 lacks direct neutralizing activity but has no
309 infectivity-enhancing properties (Figure 2A, B). The CV3-13 binding mode permits
310 effective engagement of innate immune cells to mediate Fc-effector activity. Indeed, it
311 has been shown that antibodies targeting the NTD supersite have largely overlapping
312 epitope footprints (all engaging the N1, N3 and N5 NTD loops) and a narrow range in
313 their angle of approach that could allow them to sterically disrupt spike-receptor
314 interactions, TMPRSS2-dependent activation and/or viral-host membrane fusion.
315
316 Both CV3-13 and the supersite specific Abs bind to the NTD utilizing highly mobile and
317 conformationally unconstrained NTD loops by an induced-fit mechanism. To assess the
318 impact of antibody recognition on the conformation of NTD, we superimposed the NTD
319 domain from the ligand-free HexaPro Spike (PDB:6XKL) and eleven NTD-directed
320 antibody-spike/NTD complexes and examined mAb-induced structural rearrangements.
321 As described earlier by Cerutti and colleagues (Cerutti et al., 2021), the highly mobile

N1-N5 loops (Figure 4D), which are largely disordered in the ligand-free spike, have diverse conformations in response to the bound Fabs at different sites (Figure 4E). The degree of local flexibility for the NTD loops is inversely correlated with their contribution to the Fab-NTD interface. These structural changes are a direct consequence of antibody binding, either by a conformational sampling or an induced-fit mechanism. Overall, NTD-directed antibodies induced substantial structural rearrangement of the NTD. The high immunogenicity and high mutational frequency observed in the flexible NTD loops likely results from their increased accessibility on the Spike and their subsequent encounters with both neutralizing and non-neutralizing antibodies.

CV3-13 does not protect K18-hACE2 mice from a SARS-CoV-2 lethal challenge

We next investigated the *in vivo* efficacy of the non-neutralizing antibody CV3-13 under a prophylactic or therapeutic setting to protect or treat K18-hACE2 transgenic mice from a lethal SARS-CoV-2 infection. CV3-13 was delivered intraperitoneally (ip, 12.5 mg IgG/kg body weight) 24 h before (prophylactic) or one and two days post infection (dpi, therapeutic) in K18-hACE2 mice intranasally challenged with SARS-CoV-2 nLuc, as previously described (Figure S2 and S3) (Ullah et al., 2021). Longitudinal non-invasive bioluminescence imaging (BLI), body weight change, survival, viral load estimation in brain, lung and nasal cavity and terminal imaging after necropsy showed no difference between isotype- and CV3-13-treated mice under either prophylactic or therapeutic settings (Figure S2 and S3, panels A-J). Furthermore, mRNA levels of inflammatory cytokines (*IL6, CCL2, CXCL10* and *IFNG*) in brain and lungs were also similar to isotype-treated cohorts (Figure S2 and S3, panels K, L). These data suggest that natural

Fc-effector functions associated with CV3-13 are not enough to alter virus replication and dissemination *in vivo* in the stringent K18-hACE2 mouse model of SARS-CoV-2 infection. Thus, in addition to clearing infected cells by engaging innate immune cells through Fc, efficient Fab-mediated neutralization of free viruses is essential for optimal *in vivo* efficacy. A compromise in either function reduces antibody-mediated protection *in vivo*.

Fc-effector function enhancing mutations in CV3-13 delay neuroinvasion and mortality in a prophylactic regimen in K18-hACE2 mice

We explored if introducing Fc-effector function enhancing mutations (GASDALIE) in CV3-13 can improve *in vivo* efficacy against SARS-CoV-2. As shown in Figure 2, introduction of the GASDALIE mutations significantly enhanced Fc-mediated effector functions without affecting the lack of neutralizing activity of CV3-13. We carried out temporal BLI to visualize the viral dissemination profile when a CV3-13 GASDALIE mutant was administered under the prophylactic regimen in SARS-CoV-2-nLuc challenged K18-hACE2 mice (Figure 5A). Non-invasive imaging analyses revealed that CV3-13 GASDALIE-pre-treated mice showed reduced viral spread and delayed neuroinvasion compared to isotype-treated controls (Figure 5B, D, E). Accordingly, CV3-13 GASDALIE-treated mice displayed a decelerated body-weight loss phenotype and a significant delay in mortality (Figure 5F, G). Imaging animals at the experimental endpoint after necropsy revealed that systemic virus spread as measured by flux as well as viral loads in the nose, brain and lungs were significantly reduced in CV3-13

368 GASDALIE-treated compared to isotype-treated mice (Figure 5B, C, H-J). While the
369 overall inflammatory cytokine mRNA expression profile in the brain and lungs were not
370 different, IFN-gamma mRNA levels were significantly reduced in the brain tissues of
371 CV3-13 GASDALIE-treated mice as compared to controls.
372
373 To confirm the ability of CV3-13 GASDALIE to reduce virus spread and delay
374 neuroinvasion, we terminated the experiment at 4 dpi (Figure 6A). Our BLI analyses
375 confirmed a significant decrease in nLuc signals in the brain both non-invasively and
376 after necropsy (Figure 6B-E, G, H). Viral burden measurements by assessing
377 Nucleocapsid mRNA levels and nLuc activity from Vero ACE2-TMPRSS2 infected with
378 tissue homogenates as well as histological analyses corroborated a significant reduction
379 of viral replication in the brains of CV3-13 GASDALIE-treated mice (Figure 6B-E, G-
380 K). While viral loads and cytokine mRNA levels in the lungs were similar between the
381 two cohorts, there was a significant decrease in overall inflammatory cytokine mRNA
382 levels in the brain consistent with reduced viral loads in CV3-13 GASDALIE-treated
383 mice (Figure 6L, M). Thus, these data demonstrate the potential of non-neutralizing
384 antibodies with enhanced Fc-effector functions to interfere with SARS-CoV-2 spread.
385
386
387

Discussion

Neutralization plays a crucial role in protection against SARS-CoV-2 infection. Therefore many studies have focused on neutralization responses from convalescent plasma (Anand et al., 2021; Beaudoin-Bussieres et al., 2020; Gasser et al., 2021; Long et al., 2020; Prevost et al., 2020; Robbiani et al., 2020), vaccine-elicited antibodies (AstraZeneca and Iqvia Pty, 2021; Baden et al., 2021; Bio and Pfizer, 2021; Janssen and Prevention, 2021; ModernaTx et al., 2022; Polack et al., 2020; Skowronski and De Serres, 2021; Tauzin et al., 2021) and cocktails of mAbs for use as therapeutics (Hurlburt et al., 2020; Jennewein et al., 2021; Ju et al., 2020; Li et al., 2021b; Liu et al., 2020; Schafer et al., 2021; Tian et al., 2020; Wu et al., 2020c; Yuan et al., 2020). However, antibodies are polyvalent molecules able to mediate several antiviral functions (Adeniji et al., 2021). Among these, their capacity to recognize antigens at the surface of viral particles or infected cells and to recruit effector cells is gaining attention for SARS-CoV-2 infection (Brunet-Ratnasingham et al., 2021; Schafer et al., 2021; Tortorici et al., 2020; Ullah et al., 2021; Winkler et al., 2021; Zohar et al., 2020). Also, recent studies on vaccine-elicited humoral responses suggest that additional mechanisms, besides neutralization, could be playing a role in vaccine efficacy (Alter et al., 2021; Amanat et al., 2021; Stankov et al., 2021; Tauzin et al., 2021). To address whether a non-neutralizing antibody can afford any level of protection from SARS-CoV-2 infection, we isolated a non-neutralizing antibody, CV3-13, from a convalescent donor and assessed its impact on the virus. CV3-13 binds the NTD of the Spike with high affinity and defines a novel NTD epitope. As compared to other NTD-supersite-directed neutralizing mAbs which bind the NTD predominately through use of the N1, N3 and N5 loops and

411 approach the NTD from the top, CV3-13 targets the lateral NTD surface, engaging and
412 rearranging a new set of antigenic NTD loops: N2, N4 and N2-3. The NTD interface
413 residues, as identified by the cryo-EM structure, harbor frequent mutations in several
414 circulating SARS-CoV-2 variants, including B.1.1.7 (alpha), B.1.617.1 (kappa), and C.37
415 (lambda), defining the structural basis for viral escape from CV3-13 and CV3-13-like
416 antibodies. For instance, Tyr^{144} on the protruding N3 loop, forms close contact with the
417 Tyr/Phe-rich CDR H3 of CV3-13 (Figure 3D), and is deleted in B.1.1.7, which markedly
418 reduces its binding to CV3-13 (Figure 1A). Other NTD mutations outside of the supersite
419 are found within the CV3-13 epitope including an N2 deletion $^{69}HisVal^{70}$ in B.1.1.7, a
420 Gly^{75} to Val/Thr^{76} to Ile double mutation in C.37, and a recurrent Thr^{95} to Ile mutation in
421 B.1.526 and B.1.617.1 (Figure S6A). This is in line with the interpretation that NTD
422 mutations from the emerging variants may be a result of NTD-directed antibody
423 selection, suggesting that non-neutralizing NTD antibodies like CV3-13 influence virus
424 evolution through the Fc-mediated effector functions.
425
426 CV3-13 did not neutralize pseudoviral particles or authentic SARS-CoV-2 viruses but did
427 mediate Fc effector functions against Spike-expressing cells. We suggest that differences
428 in fine epitope specificity and the angle of approach used by CV3-13 as compared to
429 neutralizing NTD-specific mAbs limit its ability to sterically hinder Spike-co-
430 receptor/auxiliary receptor interactions, the prefusion-to-postfusion transition of Spike
431 and/or membrane fusion as has been suggested as a neutralization mechanism for other
432 NTD binding antibodies.

Our data demonstrates that an antibody devoid of neutralizing activity is able to reduce virus dissemination and delay death in mice from lethal SARS-CoV-2 challenge via its Fc-mediated effector functions. While wild-type CV3-13 IgG1 did not provide any protection, CV3-13 GASDALIE mutant delayed death in prophylactically treated mice. These data suggest that a threshold of Fc-mediated effector function activity was required to impede virus progression.

While non-neutralizing antibodies do not directly inactivate free viruses, they remain attractive candidates for eliminating infected cells through Fc engagement and reduce virus burden. Although the characteristics including binding efficiency and angle of approach for efficient elimination of infected cells by non-neutralizing antibodies remains to be elucidated, here we show that enhancing Fc mutations (GASDALIE) are a crucial step in improving in vivo efficacy.

Altogether, CV3-13 represents of a new class of non-neutralizing NTD-directed mAbs that can mediate Fc-effector functions both *in vivo* and *in vitro*. Our data indicates that in addition to neutralization, additional antibody properties including Fc-mediated effector functions contribute to limiting viral spread and aid in fighting SARS-CoV-2 infection.

Supplemental information

6 Supplementary figures and 1 table.

Author contributions

GBB, YC, PDU, MP & AF : Conceptualization, Experimental design, Interpretation, Manuscript preparation and Writing; GBB : Generation of the GASDALIE and LALA mutants, Figure generation, Data processing and Initial draft; IU: Animal experiments, BLI, Viral load analyses, Data processing and Figure generation; YC, EP, WT, MP & FZ: Cryo-EM data collection, processing and validation; YC, WT & MP: Structural analysis and Figure generation; PDU: Histological analyses and Figure generation; GBB, JP, MB, SYG, SD, RG, YC, AT, GG, LS, DV, DC, ATM, JR, MP, WM & AF: Isolation, generation and characterization of SARS-CoV-2 S mAb CV3-13; SYG, JP & DV : Generation of the individual B.1.1.7 mutations in the Spike; MR & HC: Provided authentic SARS-CoV-2 virus; PK, MP, PDU, WM & AF: Funding for the work. Every author has read, edited, and approved the final manuscript.

Acknowledgements

The authors thank the CRCHUM BSL-3 and Flow Cytometry Platforms for technical assistance. We thank Dr. Stefan Pöhlmann and Dr. Markus Hoffmann (Georg-August University) for the plasmids coding for SARS-CoV-2 and SARS-CoV-1 S and Dr. M. Gordon Joyce (U.S. MHRP) for the CR3022 mAb. Antibodies CV3-1, CV3-13 and CV3-25 were produced using the pTT vector kindly provided by the National Research Council of Canada. Schematics for showing experimental design in figures were created

with BioRender.com. This work was supported by le Ministère de l'Économie et de l'Innovation (MEI) du Québec, Programme de soutien aux organismes de recherche et d'innovation, the Fondation du CHUM, a CIHR foundation grant #352417, an Exceptional Fund COVID-19 from the Canada Foundation for Innovation (CFI) #41027, a CIHR operating grant Pandemic and Health Emergencies Research/Project #177958 and a CIHR stream 1 and 2 for SARS-CoV-2 Variant Research to A.F. Support was also provided by the Sentinelle COVID Quebec network led by the Laboratoire de Santé Publique du Quebec (LSPQ) in collaboration with Fonds de Recherche du Québec-Santé (FRQS) and Genome Canada – Génome Québec, and by the Ministère de la Santé et des Services Sociaux (MSSS) and MEI to A.F. and M.R. NIH grant R01AI163395 to W.M. A.F. is recipient of a Canada Research Chair on Retroviral Entry no. RCHS0235 950-232424. G.B.B. is the recipient of CIHR and FRQS PhD fellowships and J.P. is the recipient of a CIHR PhD fellowship. RG is supported by a MITACS Accélération postdoctoral fellowship. The funders had no role in study design, data collection and analysis, decision to publish, or preparation of the manuscript. CryoEM data were collected at the Maryland Center for Advanced Molecular Analyses which is supported by MPOWER (The University of Maryland Strategic Partnership).

Disclaimer

The views expressed in this presentation are those of the authors and do not reflect the official policy or position of the Uniformed Services University, the U.S. Army, the Department of Defense, or the U.S. Government.

497

498 **Declaration of Interests**

499 LS, ATM and AF have filed a provisional patent application on the following monoclonal

500 antibodies: CV3-1, CV3-13 and CV3-25.

Figure Legends

Figure 1. Recognition of SARS-CoV-2 Spikes by CV3-13.

(A) Staining of CV3-13 (5 µg/mL) on the Spike of the WT (Wuhan-Hu-1) or the B.1.1.7 (alpha variant) strain of SARS-CoV-2 expressed at the surface of 293T transfected cells. (B) Staining of CV3-13 (5 µg/mL) on the different individual mutations of the Spike of the B.1.1.7 strain of SARS-CoV-2 (D614G, Δ69-70, Δ144, N501Y, A570D, P681H, T716I, S982A and D1118H). CV3-13 binding was further normalized to the binding obtained with the conformational-independent CV3-25 mAb (5 µg/mL). Statistical significance was evaluated using a non-parametric Mann-Whitney U test (**, $p < 0.01$). Data are the average of the median of each experiment done at least 2 times. Mean values ± Standard error of the mean (SEM). (C) SPR-based epitope mapping reveals that CV3-13 explicitly binds to SARS-CoV-2 spike S1 subunit. Different viral antigens from SARS-CoV or SARS-CoV-2 were injected to the immobilized CV3-13 IgG (~5800 RU) at the indicated concentrations. (D) Kinetics measurement of CV3-13 Fab binding to the immobilized SARS-CoV-2 HexaPro spike (~800 RU) with concentrations ranging from 3.125 to 200 nM (2-fold serial dilution). The experimental data (red) were fitted to a 1:1 Langmuir model (black) in BIA evaluation software.

Figure 2. CV3-13 is a non-neutralizing antibody that has potent Fc-mediated effector functions.

(A) Neutralizing activity of titrated concentrations of CV3-13 WT, CV3-13 LALA, CV3-13 GASDALIE and CV3-1 on SARS-CoV-2 Spike D614G bearing pseudoviruses using 293T-ACE2 target cells. (B) Neutralizing activity of CV3-13 WT, CV3-13 LALA, CV3-

13 GASDALIE and CV3-1 on SARS-CoV-2 D614G authentic virus using Vero E6 target cells. (C) Binding of CR3022, CV3-1, and CV3-13 WT on the surface of Vero E6 cells infected with authentic SARS-CoV-2 virus 48 hours post-infection. Intracellular Nucleocapsid (N) staining was done to separate infected from the uninfected cells. (D) Binding of CV3-13 WT, CV3-13 LALA, CV3-13 GASDALIE and CV3-1 on CEM.NKr.Spike. (E) % ADCC in the presence of titrated amounts of CV3-13 WT, CV3-13 LALA, CV3-13 GASDALIE and CV3-1 using a 1:1 ratio of parental CEM.NKr cells and CEM.NKr-Spike cells as target cells while PBMCs from uninfected donors were used as effector cells. (F) % ADCP in the presence of titrated amounts of CV3-13 WT, CV3-13 LALA, CV3-13 GASDALIE and CV3-1 using CEM.NKr-Spike cells as target cells and THP-1 cells as phagocytic cells. Data are the average of at least 2 experiments for (A), (B), (D)-(F). Data is from a single experiment for (C). Mean values ± SEM.

Figure 3. Cryo-EM structure of SARS-CoV-2 Spike in complex with CV3-13 Fab.

(A) Side and top views of the NTD-targeting CV3-13 Fab and SARS-CoV-2 Spike complex reveal a symmetrical Fab-spike assembly. In the left panel, protomer A of the Spike colored in salmon is shown in ribbons while the other two protomers colored in green or grey and the variable regions (heavy chain - light yellow and light chain - cyan) of three CV3-13 Fabs binding to the lateral surface of the NTD are shown as cryo-EM density (C3-symmetry map). (B) The total buried surface area (BSA) at the Fab/NTD interface contributed by heavy/light chains of CV3-13 and eleven other structurally available NTD-directed mAbs,:4A8 (PDB: 7CL2), S2M28 (7LY3), S2L28 (7LXX), 5-24 (7L2F), 4-18 (7L2E), 4-8 (7LQV), 1-87 (7L2D), 2-51 (7L2C), CM25 (7M8J), FC05

(7CWS) and DH1052 (7LAB). The BSA values of all the equivalent biological assemblies were calculated and averaged by PISA (Krissinel and Henrick, 2007). (C) Expanded view of CV3-13 interactions with the protruding NTD loops. CV3-13 is shown as surface with the CDRs H1, H2, H3 L1, L2 and L3 colored in yellow, orange, gold, dark cyan, sky blue and deep blue respectively. The NTD regions are displayed as ribbons and the N1 to N5 loops as defined by (Chi et al., 2020) are colored in green, purple, deep red, blue and pink respectively. Of note, the newly identified N2-3 hairpin is highlighted in light green. (D) CV3-13 epitope footprint on the electrostatic potential surface of NTD (colored red, blue and white for negative, positive and neutral electrostatic potential respectively). The NTD residues interacting with CV3-13, which were defined as those with BSA > 0 $Å^2$ as calculated by PISA, are colored as in (C) in accordance with loop locations. The CV3-13 epitope footprints is outlined in green. The deleted Y^{144} identified in B.1.1.7 variant that disrupts CV3-13 binding is marked with a red box.

Figure 4. Structural basis of SARS-CoV-2 Spike recognition by CV3-13 and NTD-directed neutralizing mAbs.

(A) Two-view diagram of CV3-13 binding to the NTD lateral epitope as compared to 11 other NTD-targeting neutralizing mAbs and 3 other infectivity enhancing mAbs. The NTD defined in this study is used here and shown as a light blue surface with the NTD supersite (residues 14-20, 140-158 and 245-264) highlighted in blue. On the left panel, the CV3-13 variable region is shown as a surface in light yellow for heavy chain and cyan for light chain. The approach of other NTD-binding mAbs are graphically

represented by arrows (using the average Cα position of the variable region for individual NTD-targeting antibodies ($C\alpha\text{-}_{Fv}$) pointing toward the average Cα position of the NTD domains as a whole ($C\alpha\text{-}_{NTD}$) determined by individual NTD/spike-mAb complexes) in indicated colors. On the right panel, the NTD is shown in semi-transparent surface with NTD loops N1-N5 and the newly defined N2-3 hairpin shown as colored ribbons. The CV3-13 epitope boundary is shown with a green line. The Cα-Fv of each NTD antibody is shown as colored spheres. (B) Angles of approach of CV3-13 and other NTD antibodies. The values for individual mAbs are calculated as the angle between $C\alpha\text{-}_{Fv}$ and $C\alpha\text{-}_{NTD}$ with $C\alpha_{\text{-NTD-Cter}}$ acting as the origin. (C) Diagram of NTD-antibody epitopes reveal a distinct set of CV3-13 interacting NTD residues. The buried surface area (BSA) for the NTD residues contacting individual mAbs were calculated by PISA. (D) B-factor representation of the CV3-13-bound NTD domain. (E) Orthogonal views of the NTD superimposition of reported EM/X-ray structures of NTD-binding mAbs in complex with SARS-CoV-2 spike or NTD. On the left panel, N1-N5 loops and N2-3 hairpin of CV3-13-bound NTD are shown as colored ribbons with the NTD scaffold is colored in yellow, while the other NTDs are uniformly depicted as grey ribbons. In the right panel, CV3-13-bound NTD is shown by yellow ribbons and the antigen NTD loops from other mAb-NTD structures are shown with colored ribbons with the scaffold colored in grey.

Figure 5. Prophylactic treatment with CV3-13 GASDALIE reduces SARS-CoV-2 spread and delays mortality in K18-hACE2 mouse model

(A) Experimental design for testing *in vivo* efficacy of Fc-effector function enhanced CV3-13 GASDALIE 1 day prior to challenging K18-hACE2 mice (i.n.) with SARS-CoV-2-nLuc followed by non-invasive BLI every 2 days. Human IgG1-treated (12.5 mg IgG/kg) mice were use as the isotype control (Iso) (B) Representative images from BLI of SARS-CoV-2-nLuc-infected mice in ventral (v) and dorsal (d) positions at the indicated dpi and after necropsy for experiment as in A. (C) *Ex-vivo* quantification of nLuc signal as flux (photons/sec) after necropsy. (D, E) Temporal quantification of nLuc signal as flux (photons/sec) computed non-invasively in indicated areas of each animal. (F) Temporal changes in mouse body weight with initial body weight set to 100 %. (G) Kaplan-Meier survival curves of mice statistically compared by log-rank (Mantel-Cox) test for experiment as in A. (H, I) *Ex-vivo* imaging of indicated organs and quantification of nLuc signal as flux (photons/sec) at the indicated dpi after necropsy. (J) Viral loads (nLuc activity/g) from indicated organs using Vero E6 cells as targets. (K, L) Cytokine mRNA levels in lung and brain tissues after necropsy normalized to *Gapdh* in the same sample and that in uninfected mice. Viral loads (J) and inflammatory cytokine profile (K, L) were determined after necropsy for mice when they succumbed to infection. Scale bars in (B) and (H) denote radiance (photons/sec/cm^2/steradian). Each curve in (D)-(F) and each data point in (C, I)-(L) represents an individual mouse. The data in (C), (I)-(L) were analyzed by Mann Whitney U test. Statistical significance to isotype control are shown. $*$, $p < 0.05$; $**$, $p < 0.01$;1; Mean values ± SD are depicted.

Figure 6. CV3-13 GASDALIE delays neuroinvasion and reduces inflammation in the brain of SARS-CoV-2-challenged K18-hACE2 mice.

(A) Experimental design for testing virus dissemination in CV3-13 GASDALIE administered K18-hACE2 mice, 1 day prior to challenging (i.n.) with SARS-CoV-2-nLuc followed by non-invasive BLI every 2 days. Human IgG1-treated (12.5 mg IgG/kg) mice were use as the isotype control (Iso). (B) Representative images from BLI of SARS-CoV-2-nLuc-infected mice in ventral (v) and dorsal (d) positions at the indicated dpi and after necropsy at indicated days for experiment as in A. (C) *Ex-vivo* quantification of nLuc signal as flux (photons/sec) at 4 dpi after necropsy. (D, E) Temporal quantification of nLuc signal as flux (photons/sec) computed non-invasively in indicated areas of each animal. (F) Temporal changes in mouse body weight with initial body weight set to 100%. (G, H) *Ex-vivo* imaging of organs and quantification of nLuc signal as flux (photons/sec) at the indicated dpi after necropsy. (I) A plot showing real-time PCR analyses to detect SARS-CoV-2 nucleocapsid (N) gene mRNA in indicated organs at 4 dpi. The data were normalized to N RNA seen in uninfected mice and GAPDH mRNA levels. (J) Viral loads (nLuc activity/g) from indicated organs using Vero E6 cells as targets. (K) Images of cryosections from brain tissues of SARS-CoV-2-nLuc infected K18-hACE2 mouse treated with indicated antibodies and harvested at 4 dpi. Actin (blue) was detected using phalloidin-CF450, nucleocapsid (green) was detected using anti-SARS-CoV-2 N conjugated to AF488. Scale bar 150 µm. (L, M) Cytokine mRNA levels in lung and brain tissues after necropsy normalized to *Gapdh* in the same sample and that in uninfected mice. Viral loads (J) and inflammatory cytokine profile (L, M) were determined after necropsy for mice that succumbed to infection. Scale bars in (B) and (G) denote radiance (photons/sec/cm^2/steradian). Each curve in (D)-(F) and each data point in (C), (H)-(J), (L) and (M) represents an individual mouse. The data in (C), (H)-(J), (L) and

638 (M) were analyzed by Mann Whitney U test. Statistical significance to isotype control are

639 shown. $*$, $p < 0.05$; $**$, $p < 0.01$; Mean values ± SD are depicted.

Supplementary Figure Legends:

Figure S1. LALA and GASDALIE Fc mutations does not affect CV3-13 binding to SARS-CoV-2 Spike.

(A) Indirect ELISA on SARS-CoV-2 Spike 6P using CV3-13 WT, CV3-13 LALA, CV3-13 GASDALIE, CV3-1, CV3-25 and CR3022 (50 ng/mL). CR3022 was used as a positive control in each ELISA plate and for each experiment the data was further normalized on the signal obtained with this antibody. Experiment was done 4 times. (B) Staining with CV3-13 WT, CV3-13 LALA, CV3-13 GASDALIE, CV3-1, CV3-25 and CR3022 (5 µg/mL) of 293T cells transfected with the SARS-CoV-2 Spike. CR3022 was used as a positive control in each experiment and for each experiment the data was further normalized on the signal obtained with this antibody. Experiment was done 3 times. Statistical significance was evaluated using a non-parametric Mann-Whitney U test (n.s., not significant). The data shown is the mean ± SEM.

Figure S2. Prophylactic treatment with non-neutralizing CV3-13 antibody does not protect K18-hACE2 mice from lethal SARS-CoV-2 infection

(A) Experimental design for testing *in vivo* efficacy of non-neutralizing CV3-13 antibody administered 1 day prior to challenging K18-hACE2 mice (i.n.) with SARS-CoV-2-nLuc followed by non-invasive BLI every 2 days. Human IgG1-treated (12.5 mg IgG/kg) mice were use as the isotype control (Iso). (B) Representative images from BLI of SARS-CoV-2-nLuc-infected mice in ventral (v) and dorsal (d) positions at the indicated dpi and after necropsy for experiment as in A. (C) *Ex-vivo* quantification of nLuc signal as flux (photons/sec) after necropsy. (D, E) Temporal quantification of nLuc signal as flux

(photons/sec) computed non-invasively in indicated areas of each animal. (F) Temporal changes in mouse body weight with initial body weight set to 100 %. (G) Kaplan-Meier survival curves of mice statistically compared by log-rank (Mantel-Cox) test for experiment as in A. (H, I) *Ex-vivo* imaging of organs and quantification of nLuc signal as flux (photons/sec) at the indicated dpi after necropsy. (J) Viral loads (nLuc activity/g) from indicated organs using Vero E6 cells as targets. (K, L) Cytokine mRNA levels in lung and brain tissues after necropsy normalized to *Gapdh* in the same sample and that in uninfected mice. Viral loads (J) and inflammatory cytokine profile (K, L) were determined after necropsy for mice that succumbed to infection. Scale bars in (B) and (H) denote radiance (photons/sec/cm^2/steradian). Each curve in (D)-(F) and each data point in (C) and (I)-(L) represents an individual mouse. The data in (C) and (I)-(L) were analyzed by non-parametric Mann Whitney test. Non-significant values are not shown, Mean values ± SD are depicted.

Figure S3. Therapeutic treatment with non-neutralizing CV3-13 antibody does not protect K18-hACE2 mice from lethal SARS-CoV-2 infection

(A) Experimental design for testing *in vivo* efficacy of CV3-13 administered at 1 and 2 dpi after challenging K18-hACE2 mice (i.n.) with SARS-CoV-2-nLuc followed by non-invasive BLI every 2 days. Human IgG1-treated (12.5 mg IgG/kg) mice were use as the isotype control (Iso). (B) Representative images from BLI of SARS-CoV-2-nLuc-infected mice in ventral (v) and dorsal (d) positions at the indicated dpi and after necropsy at indicated days for experiment as in A. (C) *Ex-vivo* quantification of nLuc signal as flux (photons/sec) after necropsy. (D, E) Temporal quantification of nLuc signal

as flux (photons/sec) computed non-invasively in indicated areas of each animal. (F) Temporal changes in mouse body weight with initial body weight set to 100 %. (G) Kaplan-Meier survival curves of mice statistically compared by log-rank (Mantel-Cox) test for experiment as in A. (H, I) *Ex-vivo* imaging of organs and quantification of nLuc signal as flux (photons/sec) at the indicated dpi after necropsy. (J) Viral loads (nLuc activity/g) from indicated organs using Vero E6 cells as targets. (K, L) Cytokine mRNA levels in lung and brain tissues after necropsy normalized to *Gapdh* in the same sample and that in uninfected mice. Viral loads (J) and inflammatory cytokine profile (K, L) were determined after necropsy for mice that succumbed to infection. Scale bars in (B) and (H) denote radiance (photons/sec/cm^2/steradian). Each curve in (D)-(F) and each data point in (C) and (I)-(L) represents an individual mouse. The data in (C) and (I)-(L) were analyzed by Mann Whitney U test. Mean values ± SD are depicted.

Figure S4. Cryo-EM data collection and processing of SARS-CoV-2 HexaPro Spike-CV3-13 Fab complex

(A) Cryo-EM sample preparation. Size-exclusion chromatogram (SEC) of the purified, non-tagged SARS-CoV-2 Hexa-Pro spike (blue) and its overnight mixture with CV3-13 Fab (molar-ratio: 1:20) (red) on a superpose 6 300/10 GL column. The SEC peak-shift and SDS-PAGE validate the Fab-spike complex formation. (B) Cryo-EM data processing workflow in cryosparc and the representative raw electron micrograph. (C) Selected 2D averages for *ab initio* reconstruction. (D, E) Side and top views of the final cryo-EM density map imposed with C1 (D) or C3 symmetry (E). (F, G) The Fourier shell correlation curves indicate the overall resolution (FSC cutoff 0.143) using non-uniform

709 refinement (left panel) and the direction distribution plot of all particles used in the final
710 refinement (right panel) for the C1-symmetry map (F) and the C3-symmetry map (G).
711
712 **Figure S5. Cryo-EM structure validation.**
713 (A) Two views of C3-symmetry density map colored by local resolution as calculated in
714 cryoSPARC using a FSC cutoff of 0.143. (B) Blow-up view of the density corresponding
715 to the NTD-Fv portion colored by local resolution. (C) Density fit of NTD and CV3-13
716 Fv at different contour levels (Chimera X) in which the NTD framework is shown as
717 salmon ribbons with NTD loops colored as indicated and the heavy and light chain of
718 CV3-13 variable region colored in light yellow and cyan.
719
720 **Figure S6. Sequence alignments.**
721 (A) Sequence alignment of the NTD (residue 1-317) from 11 SARS-CoV-2 variants. The
722 sequence of ancestral Wuhan strain is listed on the top and the mutations from other
723 variants are listed ("X" denotes a deletion), while the remaining identical residues to the
724 Wuhan strain are shown as "·" for clarify. CV3-13 contacting residues are shaded in grey
725 with the hydrogen-bonded residues marked above the sequence ("+" for the side chain
726 and "-" for the main chain). Residues in the NTD supersite are colored in blue and the
727 recurrently deleted regions (RDR1-4), as described by McCathy and colleagues
728 (McCarthy et al., 2021), are shaded in yellow. The regions corresponding to N1-N5 loops
729 and the N2-3 hairpin are highlighted in colored dashed rectangles. The documented
730 glycosylation sites are boxed in red. The secondary structure assignment on top is derived
731 from the 4A8-spike complex (PDB: 7C2L), the first reported NTD-directed mAb-Spike

732 structure (Chi et al., 2020). (B) V_H and V_L sequence alignments of the affinity-matured
733 CV3-13 and its germline IGHV4 and IGKV1 and the other NTD-directed mAbs. The
734 NTD-contact residues are shaded in grey with those involved in hydrogen-bonds marked
735 with (+) for side chain and (-) for mainchain above the sequence. The somatically
736 mutated residues in the germline sequence are as shown with the unchanged residues
737 marked as "·".
738
739
740

741 **Supplemental table 1. Cryo-EM data collection and refinement statistics**

Protein	**SARS-CoV-2 HexaPro spike/CV3-13 Fab**
EMDB	EMD-24628
PDB	7RQ6
Data collection and Reconstruction	
Microscope	FEI Glacios
Voltage (kV)	200
Electron dose ($e^-/Å^2$)	42
Detector	Gatan K3
Magnification	45,000
Pixel size (Å/pix)	0.889
Defocus range (μm)	0.27-3.03
Micrographs collected	2,181
Particles extracted/final	916,236/98,752
Symmetry imposed	C3
Box size (pix)	512
Unmasked resolution at 0.5/0.143 FSC (Å)	4.45 / 4.22
Masked resolution at 0.5/0.143 FSC (Å)	4.37 /4.19
Refinement and Validation	
Software	CryoSPARC/Phenix 1.18/ccpEM
Protein residues	3951
Chimera CC	0.868
EMRinger Score	1.77
Model vs data CC	0.76
R.m.s. Deviations	
Bond Length (Å)	0.004
Bond Angles (^{o})	0.726
Molprobility score	2.14
Clash score	13.20
Favored rotamers (%)	99.94
Ramamchandran	
Favored regions (%)	91.34
Allowed regions (%)	8.58
Disallowed regions (%)	0.08

742

STAR Methods

KEY RESOURCES TABLE

REAGENT or RESOURCE	SOURCE	IDENTIFIER
Antibodies		
InVivoMAb human IgG1 isotype control	Bio X Cell	RRID: AB_2687817 Cat # BE0297
Cross-reactive SARS-CoV-1 monoclonal antibody CR3022	ter Meulen et al. 2006 (ter Meulen et al., 2006)	RRID: AB_2848080
CV3-1 (IgG1)	Jennewein et al. 2021 (Jennewein et al., 2021)	N/A
CV3-13 (IgG1)	Jennewein et al. 2021 (Jennewein et al., 2021)	N/A
CV3-25 (IgG1)	Jennewein et al. 2021 (Jennewein et al., 2021)	N/A
CV3-13 LALA (IgG1)	Finzi Lab, Université de Montréal	N/A
CV3-13 GASDALIE (IgG1)	Finzi Lab, Université de Montréal	N/A
Goat anti-Human IgG (H+L) Cross-Adsorbed Secondary Antibody, Alexa Fluor 647	Invitrogen	Cat # A-21445; RRID: AB_2535862
Goat anti-Human IgG Fc Cross-Adsorbed Secondary Antibody, HRP	Invitrogen	Cat # A18823; RRID: AB_2535600
Mouse anti-SARS-CoV-2 nucleocapsid (clone 1C7)	Bioss Antibodies	Cat # bsm-41411M
Alexa Fluor® 488 anti-SARS-CoV-2 nucleocapsid (mBG17)	Prévost et al. bioRxiv 2021 (Prevost et al., 2021)	N/A
Rabbit anti-SARS-CoV-2 nucleocapsid	Novus	Cat # NB100-56576
Goat anti-Human IgG Fc Cross-Adsorbed Secondary Antibody, HRP	Invitrogen	Cat # 31413; RRID : AB_429693
Bacterial and Virus Strains		
SARS-CoV-2-nLuc (strain 2019-nCoV/USA_WA1/2020)	Craig Wilen (Yale University)	K. Plante and Pei-Yong Shi, World Reference Center for Emerging Viruses and Arboviruses, University of Texas Medical Branch)
Authentic SARS-CoV-2 D614G virus (LSPQ/231457/2020)	Prévost et al. bioRxiv 2021 (Prevost et al., 2021)	N/A
Biological Samples		
Primary human peripheral blood mononuclear cells (PBMCs)	FRQS AIDS network	N/A
Chemicals, Peptides, and Recombinant Proteins		
Liberase TL Research Grade	Sigma-Aldrich	Cat# 5401020001
DNAse I recombinant, RNAse-free	Roche	Ref # 04716728001
Gibco™ RPMI 1640 medium	Thermo Fisher Scientific	Cat # 11875093
Gibco™ Dulbecco's modified Eagle's medium (DMEM)	Thermo Fisher Scientific	Cat # 11965118

Gibco™ MEM Non-essential amino acid (NEAA) solution	Thermo Fisher Scientific	Cat # 11140050
Gibco™ Penicillin-streptomycin solution (10,000 U/ml)	Thermo Fisher Scientific	Cat # 15140122
Gibco™ Dulbecco's Phosphate Buffered Saline (DPBS)	Thermo Fisher Scientific	Cat # 14190144
Gibco™ L-Glutamine (200mM)	Thermo Fisher Scientific	Cat # 25030081
Gibco™ 0.05% Trypsin-EDTA, phenol red	Thermo Fisher Scientific	Cat # 25300054
Fetal bovine serum	Atlanta Biologicals	Cat # S11550
RBC Lysis Buffer (10X)	BioLegend Inc	Cat # 420301
Bovine Serum Albumin (BSA)	Sigma-Aldrich	Cat# A9647-100G CAS: 9048-46-8
Accutase	BioLegend Inc	Cat # 423201
0.05% Trypsin-EDTA (1X)	Life Technologies	Cat # 25300-054
K3 EDTA 15% Solution	Fisher Scientific	Cat # BD 366450
Sodium pyruvate (100 mM)	Life technologies	Ref # 11360-070
2-Mercaptoethanol	Sigma-Aldrich	Cat # M3148
L-Glutamine (200mM)	Life technologies	Ref # 25030-081
Red blood cell lysis buffer-Hybri-Max	Sigma-Aldrich	Cat # R7757-100ML
Tris-buffered saline (TBS)	Thermo Fisher Scientific	Cat # BP24711
Western Lightning Plus-ECL, Enhanced Chemiluminescence Substrate	Perkin Elmer Life Sciences	Cat # NEL105001EA
Tween20	Thermo Fisher Scientific	Cat # BP337-500
Passive lysis buffer	Promega	Cat # E1941
Triton-X 100 t-octyl phenoxy polyethoxyethanol	American Bioanalytical	Cat # AB02025-00500 CAS: 9002-93-1
Paraformaldehyde (PFA)	Electron Microscopy Sciences	Cat # 19200 CAS: 30525-89-4
Rat serum	Stemcell Biotechnologies	Cat # 13551
L-lysine Monohydrochloride	Sigma-Aldrich	Cat # L1262
Sodium (meta)periodate	Sigma-Aldrich	Cat # 30323-100G CAS: 7790-28-5
Sucrose/ α-D-glucopyranosyl-β-D-fructofuranoside	americanBIO	Ref # AB01900-01000 CAS: 57-50-1
Tissue-Tek O.C.T Compound	Sakura	Cat # 4583
Fc receptor blocker	Innovex	Cat # NB335-5
Superforst® Plus microscope slides	Thermo Scientific	Cat # 4951PLUS-001
Dimethyl sulfoxide (DMSO)	Sigma-Aldrich	Cat # D2650-5X5ML CAS: 67-68-5
Sodium azide	Sigma-Aldrich	Cat # S-8032 EC No: 247-852-1
Sodium phosphate, Monobasic, Monohydrate, Crystal ($NaH_2PO_4 \cdot H_2O$)	J.T.Baker	Cat # 3818-01 CAS: 10049-21-5
Sodium phosphate, Dibasic, Anhydrous (Na_2HPO_4)	J.T.Baker	Cat # 3828-01 CAS: 7558-79-4
Glycine	American Bioanalytical	Cat # AB00730-01000 CAS: 56-40-6
The PEG-it Virus precipitation solution (5X)	System Bioscience	Cat # LV810A-1
Avicel® Pharma Grade	FMC	Cat # RC-581 NF 10.20944/preprints202005.0264.v1
Vector® TrueView® Autofluorescence Quenching Kit	Vector Laboratories	SP-8400
Puromycin dihydrochloride	Millipore Sigma	Cat # P8833
D-Luciferin potassium salt	Prolume	Cat # 306

Formaldehyde 37%	Thermo Fisher Scientific	Cat # F79-500
LIVE/DEAD Fixable AquaVivid Cell Stain	Thermo Fisher Scientific	Cat # L34957
Cell proliferation dye eFluor670	Thermo Fisher Scientific	Cat # 65-0840-85
Cell proliferation dye eFluor450	Thermo Fisher Scientific	Cat # 65-0842-85
FreeStyle 293F expression medium	ThermoFisher Scientific	Cat # 12338002
ExpiFectamine 293 transfection reagent	ThermoFisher Scientific	Cat # A14525
Protein A Sepharose CL-4B	Cytiva	Cat # 17096303
Ni-NTA agarose	Invitrogen	Cat # R90110
Papain-agarose resin	ThermoFisher Scientific	Cat # 20341
SARS-CoV-2 S1 domain C-His tag protein, from HEK293 cells	BEI Resources	NR-53798
SARS-CoV-2 S2 ectodomain C-His tag protein, from Baculovirus	BEI Resources	NR-53799
SIGMAFAST OPD	EMD Millipore	Cat # P9187
Critical Commercial Assays		
Nano-Glo Luciferase Assay System (nanoluc substrate)	Promega	Cat # N1120
Pierce™ Gaussia Luciferase Glow Assay Kit	ThermoFisher Scientific	Cat # 16160
Strep-Tactin®XT 4Flow	IBA Lifesciences	Cat # 2-5998-000
KAPA SYBR FAST qPCR Master Mix (2X) Kit	KAPA Biosystems	Cat # KK4600 and KK4601
Ambion DNase I (RNase-free)	ThermoFisher Scientific	Cat # AM2222
RNeasy Mini Kit (50)	Qiagen	Cat #/ID 74104
iScript advanced cDNA kit	Bio Rad	Cat #1725038
iQ Multiplex Powermix	Bio Rad	Cat # 1725848
iScript™ cDNA Synthesis Kit	Bio Rad	Cat # 95047-100
Deposited Data		
Experimental Models: Cell Lines		
Vero E6 (female, Chlorocebus sabaeus)	ATCC	Cat # CRL-1586; RRID: CVCL_0574
Vero E6-TMPRSS2 (female, Chlorocebus sabaeus)	Craig B. Wilen, Yale University	N/A
HEK293 (female, Homo sapiens)	ATCC	Cat # CRL-1573; RRID: CVCL_0045
HEK293T (female, Homo sapiens)	ATCC	Cat # CRL-3216; RRID: CVCL_0063
Expi293F™ GnTI- Cells (female, Homo sapiens)	ThermoFisher Scientific	Cat # A39240; RRID: CVCL_B0J7
Expi293F cells (female, Homo sapiens)	ThermoFisher Scientific	Cat # A14527; RRID: CVCL_D615
293T-ACE2 (female, Homo sapiens)	Prevost et al. 2020 (Prevost et al., 2020)	N/A
CEM.NKr-CCR5+ (female, Homo sapiens)	NIH AIDS Reagent Program	Cat # 4376; RRID: CVCL_X623
CEM.NKr-Spike (female, Homo sapiens)	Anand et al., 2021 (Anand et al., 2021)	N/A
THP-1 (male, Homo sapiens)	ATCC	Cat # TIB-202; RRID: CVCL_0006
FreeStyle 293F cells (female, Homo sapiens)	ThermoFisher Scientific	Cat # R79007; RRID: CVCL_D603
Experimental Models: Organisms/Strains		
B6.Cg-Tg(K18-ACE2)2Prlmn/J	The Jackson Laboratory	Stock No: 034860

Oligonucleotides		
SARS-CoV-2 N F: 5'-ATGCTGCAATCGTGCTACAA-3'	Yale School of Medicine, W. M. Keck Foundation, Oligo Synthesis Resource	
SARS-CoV-2 N R: 5'-GACTGCCGCCTCTGCTC-3'	Yale School of Medicine, W. M. Keck Foundation, Oligo Synthesis Resource	
Human IgG1 G236A-S239D F : 5'-CTCCTGGCGGGACCGGATGTCTTCCTCTTC-3'	Integrated DNA Technologies	N/A
Human IgG1 G236A-S239D R : 5'-GAAGAGGAAGACATCCGGTCCCGCCAGGAG-3'	Integrated DNA Technologies	N/A
Human IgG1 A330L-I332E F : 5'-GCCCTCCCACTCCCCGAAGAGAAAACCATC-3'	Integrated DNA Technologies	N/A
Human IgG1 A330L-I332E R : 5'-GATGGTTTTCTCTTCGGGGAGTGGGAGGGC-3'	Integrated DNA Technologies	N/A
Human IgG1 L234A-L235A F: 5'-CAGCACCTGAAGCCGCGGGGGGACCGTC-3'	Integrated DNA Technologies	N/A
Human IgG1 L234A-L235A R: 5'-GACGGTCCCCCCGCGGCTTCAGGTGCTG-3'	Integrated DNA Technologies	N/A
FAM-Gapdh	Bio Rad	Cat # 12001950
HEX-IL6	Bio Rad	Cat # 10031228
TEX615-CCL2	Bio Rad	Cat # 10031234
Cy5-CXCL10	Bio Rad	Cat # 10031231
Cy5.5-IFNg	Bio Rad	Cat # 10031237
Transgene Forward: GAC CCC TGA GGG TTT CAT ATA G	Yale School of Medicine, W. M. Keck Foundation, Oligo Synthesis Resource	#53437, Genotyping primers for K18-hACE2 mice. The Jackson Laboratory
Common: CAC CAA CAC AGT TTC CCA AC	Yale School of Medicine, W. M. Keck Foundation, Oligo Synthesis Resource	#53438, Genotyping primers for K18-hACE2 mice. The Jackson Laboratory
Wildtype forward: AAG TTG GAG AAG ATG CTG AAA GA	Yale School of Medicine, W. M. Keck Foundation, Oligo Synthesis Resource	#53439, Genotyping primers for K18-hACE2 mice. The Jackson Laboratory
Recombinant DNA		
pCMV-SARS-CoV-2 Spike D614G Δ19	Ullah, Prévost et al. 2021 (Ullah et al., 2021)	N/A
pCMV-SARS-CoV-2 Spike	Sino Biological	Cat # VG40589-UT
pCMV delta R8.2	Addgene	Cat #12263
HIV-1-inGluc-ΔEnv	Mothes Lab, Yale University	N/A
pCG1-SARS-CoV-2 Spike	Hoffmann et al., 2020 (Hoffmann et al., 2020)	N/A
pCG1-SARS-CoV-2 Spike D614G	Beaudoin-Bussières et al. mBio 2020 (Beaudoin-Bussieres et al., 2020)	N/A
pCG1-SARS-CoV-2 Spike D614G N501Y	Prévost et al. bioRxiv 2021 (Prevost et al., 2021)	N/A
pcDNA3.1-SARS-CoV-2 Spike B.1.1.7	Tauzin et al. CHM 2021 (Tauzin et al., 2021)	N/A
pCG1-SARS-CoV-2 Spike D614G Δ69-70	Li, Chen, Prévost et al. bioRxiv 2021 (Li et al., 2021b)	N/A

pCG1-SARS-CoV-2 Spike D614G Δ144	Li, Chen, Prévost et al. bioRxiv 2021 (Li et al., 2021b)	N/A
pCG1-SARS-CoV-2 Spike D614G A570D	Li, Chen, Prévost et al. bioRxiv 2021 (Li et al., 2021b)	N/A
pCG1-SARS-CoV-2 Spike D614G P681H	Li, Chen, Prévost et al. bioRxiv 2021 (Li et al., 2021b)	N/A
pCG1-SARS-CoV-2 Spike D614G T716I	Li, Chen, Prévost et al. bioRxiv 2021 (Li et al., 2021b)	N/A
pCG1-SARS-CoV-2 Spike D614G S982A	Li, Chen, Prévost et al. bioRxiv 2021 (Li et al., 2021b)	N/A
pCG1-SARS-CoV-2 Spike D614G D1118H	Li, Chen, Prévost et al. bioRxiv 2021 (Li et al., 2021b)	N/A
pαH-SARS-CoV-2 Spike HexaPro	Dr Jason S. McLellan, University of Texas	N/A
pcDNA3.1-SARS-CoV-2 RBD	Beaudoin-Bussieres et al., 2020b (Beaudoin-Bussieres et al., 2020)	N/A
pNL4.3 R-E- Luc	NIH AIDS Reagent Program	Cat # 3418
pIRES2-eGFP vector	Clontech	Cat # 6029-1
Software and Algorithms		
FlowJo v10.5.3	Treestar	https://www.flowjo.com/
Nikon-Elements AR Analysis v4.13 and Acquisition v4.5	Nikon	
Adobe Photoshop CC	Adobe Systems Inc	N/A
Adobe Illustrator CC	Adobe Systems Inc	N/A
BioRender (schematics in figures)	BioRender.com	N/A
CFX MaestroTM Software (qPCR analyses)	Bio-rad Inc	N/A
Graphpad Prism v9.0.1	GraphPad Software	https://www.graphpad.com/

SerialEM software package	David N. Mastronarde, University of Colorado Boulder	https://bio3d.colorado.edu/SerialEM/
IMOD software package	David N. Mastronarde, University of Colorado Boulder	https://bio3d.colorado.edu/imod/
CryoSPARC	Punjani et al., 2017 (Punjani et al., 2017)	https://cryosparc.com
Phenix	Liebschner. et al. 2019 (Liebschner et al., 2019)	https://phenix-online.org/
Coot	Emsley et al., 2010 (Emsley et al., 2010)	https://www2.mrc-lmb.cam.ac.uk/personal/pemsley/coot/
Relion	Scheres and Chen, 2012; Zivanov et al., 2019 (Scheres and Chen, 2012) (Zivanov et al., 2018)	https://www2.mrc-lmb.cam.ac.uk/relion/index.php?title=Main_Page
UCSF ChimeraX	Goddard et al., 2018 (Goddard et al., 2018)	https://www.rbvi.ucsf.edu/chimerax/
UCSF Chimera	Goddard et al., 2007 (Goddard et al., 2007)	http://plato.cgl.ucsf.edu/chimera RRID: SCR_004097
PyMOL	The PyMOL Molecular Graphics System	https://www.schrodinger.com/products/pymol
MolProbity	Chen et al., 2010 (Chen et al., 2010)	http://molprobity.biochem.duke.edu/
PISA	Krissinel, et al., 2007 (Krissinel and Henrick, 2007)	https://www.ebi.ac.uk/pdbe/pisa/
Gen5 microplate reader and imager software	Biotek	N/A
BIAevaluation software	GE Healthcare	Cat # BR-1005-97
Other		
TriStar LB 941 Multimode Microplate Reader and Luminometer	BERTHOLD TECHNOLOGIES GmbH & Co. KG	Finzi and Mothes Lab
BD LSR II Flow Cytometer	BD Biosciences	https://medicine.yale.edu/immuno/flowcore/
Leica Cryostat CM1950	Leica	CM1950 (Iwasaki Lab; Yale Unviersity)
Nikon W1 Spinning Disk Confocal microscope	Nikon Instruments Inc, Americas	Yale West Campus Imaging Core
C1000 Touch thermal cycler	Bio-Rad	
CFX Connect™ Real-Time PCR Detection System	Bio-Rad	
Nanodrop Spectrophotometer ND-1000	ThermoFisher Scientific	
27G × ½" insulin syringe with needle	TERUMO	Cat # SS*05M2713
31G insulin syringe	BD Biosciences	Cat # 328468
70 µm Nylon cell strainer	FALCON	Cat # 352350
Acrodisc 25 mm Syringe Filter w/0.45 µm HT Tuffryn Membrane	PALL Life Sciences	Cat # 4184
Superfrost Plus Microscope Slides	Thermo Scientific	Cat # 4951PLUS-001
96-well white plates for luciferase assays	Costar	Cat # 3917
Accu-Edge High Profile Microtome Blades	SAKURA	Cat # 4685
Microcover glasses 1 ounce No.1	VWR	Cat # 48393 106
Tissue-Tek Cryomold	SAKURA	Ref # 4557
Brass planchettes	Ted Pella, Inc.	Type A and Type B

Cryotubes	Thermo Scientific Nunc	Cat # 340711
Teflon-coated glass microscope slides		
Microsurgical scalpel	Electron Microscopy Sciences	Cat # 72047-15
Plastic sectioning stubs	Home Made	
Diamond knife	Diatome, Ltd	
Formvar-coated copper-rhodium slot grids	Electron Microscopy Sciences	
Dual-axis tomography holder	E.A. Fischione Instruments, Export PA	Model 2040
Polystyrene Round-bottom Tube	FALCON	Ref # 352058
Optical Flat 8-Cap Strips for 0.2 ml tube stripes/plates	Bio-Rad	Cat # TCS0803
Individual PCR tubes 8-tube Strip, clear	Bio-Rad	Cat # TLS0801
ThermalGrid Rigid Strip PCR tubes	Denville Scientific INC	Ref # C18064
96 well U bottom plate	FALCON	Ref # 353077
XIC-3 animal isolation chamber	PerkinElmer	
IVIS Spectrum	PerkinElmer	Yale University ABSL-3 facility
RAS-4 Rodent Anesthesia System	PerkinElmer	CLS146737
QUANTIFOIL® holey carbon grids	Electron Microscopy Sciences	Cat # Q250-CR1
Synergy LX multi-mode reader	Biotek	N/A
Superose 6 10/300 GL	GE Healthcare	Cat # 17517201
Hiload 16/600 Superdex 200pg	GE Healthcare	Cat # 28989335
Biacore 3000	GE Healthcare	N/A
Protein A sensor chip	Cytiva	Cat # 29127558
Ni-NTA sensor chip	Cytiva	Cat # BR100034

747

RESOURCE AVAILABILITY

Lead Contact

Further information and requests for resources and reagents should be directed to and will be fulfilled by the Lead Contact, Andrés Finzi (andres.finzi@umontreal.ca).

Materials Availability

All other unique reagents generated in this study are available from the corresponding authors with a completed Materials Transfer Agreement.

Data and Code Availability

The data that support the findings of this study are available from the corresponding authors upon reasonable request.

EXPERIMENTAL MODEL AND SUBJECT DETAILS

Cell and Viruses

Vero E6 (CRL-1586, American Type Culture Collection (ATCC) or Vero E6-TMPRSS2 (Craig B. Wilen, Yale University), were cultured at 37°C in RPMI supplemented with 10% fetal bovine serum (FBS), 10 mM HEPES pH 7.3, 1 mM sodium pyruvate, 1× non-essential amino acids, and 100 U/ml of penicillin–streptomycin. The 2019n-CoV/USA_WA1/2019 isolate of SARS-CoV-2 expressing nanoluciferase was obtained from Craig Wilen, Yale University and generously provided by K. Plante and Pei-Yong Shi, World Reference Center for Emerging Viruses and Arboviruses, University of Texas

771 Medical Branch) (Xie et al., 2020a; Xie et al., 2020b). Virus was propagated in Vero-E6
772 or Vero E6-TMPRSS2 by infecting them in T150 cm^2 flasks at a MOI of 0.1. The culture
773 supernatants were collected after 72 h when cytopathic effects were clearly visible. The
774 cell debris was removed by centrifugation and filtered through 0.45-micron filter to
775 generate virus stocks. Viruses were concentrated by adding one volume of cold (4 °C) 4x
776 PEG-it Virus Precipitation Solution (40 % (w/v) PEG-8000 and 1.2 M NaCl; System
777 Biosciences) to three volumes of virus-containing supernatant. The solution was mixed
778 by inverting the tubes several times and then incubated at 4 °C overnight. The
779 precipitated virus was harvested by centrifugation at 1,500 × g for 60 minutes at 4 °C.
780 The concentrated virus was then resuspended in PBS then aliquoted for storage at −80°C.
781 All work with infectious SARS-CoV-2 was performed in Institutional Biosafety
782 Committee approved BSL3 and A-BSL3 facilities at Yale University School of Medicine
783 or Université de Montréal using appropriate positive pressure air respirators and
784 protective equipment. CEM.NKr, CEM.NKr-Spike, THP-1 and peripheral blood
785 mononuclear cells (PBMCs) were maintained at 37°C under 5% CO_2 in RPMI media,
786 supplemented with 10% FBS and 100 U/mL penicillin/streptomycin. 293T (or
787 HEK293T) and 293T-ACE2 cells were maintained at 37°C under 5% CO_2 in DMEM
788 media, supplemented with 5% FBS and 100 U/mL penicillin/streptomycin. CEM.NKr
789 (NIH AIDS Reagent Program) is a T lymphocytic cell line resistant to NK cell-mediated
790 lysis. CEM.NKr-Spike stably expressing SARS-CoV-2 Spike were used as target cells in
791 ADCC and ADCP assays (Anand et al., 2021). THP-1 monocytic cell line (ATCC) was
792 used as effector cells in the ADCP assay. PBMCs were obtained from healthy donor
793 through leukapheresis and were used as effector cells in ADCC assay. 293T cells

(obtained from ATCC) were derived from 293 cells, into which the simian virus 40 T-antigen was inserted. 293T-ACE2 cells stably expressing human ACE2 is derived from 293T cells (Prevost et al., 2020). 293T-ACE2 cells were cultured in medium supplemented with 2 mg/mL of puromycin (Millipore Sigma).

Ethics statement

PBMCs from healthy individuals as a source of effector cells in our ADCC assay were obtained under CRCHUM institutional review board (protocol #19.381). Research adhered to the standards indicated by the Declaration of Helsinki. All participants were adults and provided informed written consent prior to enrollment in accordance with Institutional Review Board approval.

Antibodies

The human antibodies (CV3-1, CV3-25 and CV3-13) used in the work were isolated from blood of male convalescent donor CV3 recovered 41 days after symptoms onset using fluorescent recombinant stabilized Spike ectodomains (S2P) as probes to identify antigen-specific B cells as previously described (Lu et al., 2020; Seydoux et al., 2020). Light and heavy chains were cloned into the pTT expression plasmid (Durocher et al., 2002). Site-directed mutagenesis was performed on plasmids expressing CV3-13 antibody heavy chains in order to introduce the LALA mutations (L234A/L235A) and the GASDALIE mutations (G236A/S239D/A330L/I332E) using to the QuickChange II XL site-directed mutagenesis protocol (Stratagene).

817

818 **Mouse Experiments**

819 All experiments were approved by the Institutional Animal Care and Use Committees
820 (IACUC) of and Institutional Biosafety Committee of Yale University (IBSCYU). All the
821 animals were housed under specific pathogen-free conditions in the facilities provided
822 and supported by Yale Animal Resources Center (YARC). All IVIS imaging, blood draw
823 and virus inoculation experiments were done under anesthesia using regulated flow of
824 isoflurane:oxygen mix to minimize pain and discomfort to the animals.

825

826 **METHOD DETAILS**

827 **SARS-CoV-2 infection and treatment conditions**

828 For all *in vivo* experiments, the 6 to 8 weeks male and female hACE2-K18 mice were
829 intranasally challenged with 1 x 10^5 PFU in 25-30 µl volume under anesthesia (0.5 - 5 %
830 isoflurane delivered using precision Dräger vaporizer with oxygen flow rate of 1 L/min).
831 For mAb treatment using prophylaxis regimen, mice were treated with 250 µg (12.5 µg/g
832 body weight) of indicated antibodies (CV3-13 WT or CV3-13 GASDALIE) via
833 intraperitoneal injection (i.p.) 24 h prior to infection. For mAb treatment under
834 therapeutic regimen, mice were treated at 1 and 2 dpi intraperitoneally with CV3-13 (12.5
835 µg/g body weight). Body weight was measured and recorded daily. The starting body
836 weight was set to 100 %. For survival experiments, mice were monitored every 6-12 h
837 starting six days after virus administration. Lethargic and moribund mice or mice that had
838 lost more than 20 % of their body weight were sacrificed and considered to have
839 succumbed to infection for Kaplan-Meier survival plots.

840

841 **Bioluminescence Imaging (BLI) of SARS-CoV-2 infection**

842 All standard operating procedures and protocols for IVIS imaging of SARS-CoV-2
843 infected animals under ABSL-3 conditions were approved by IACUC, IBSCYU and
844 YARC. All the imaging was carried out using IVIS Spectrum® (PerkinElmer) in XIC-3
845 animal isolation chamber (PerkinElmer) that provided biological isolation of anesthetized
846 mice or individual organs during the imaging procedure. All mice were anesthetized via
847 isoflurane inhalation (3 - 5 % isoflurane, oxygen flow rate of 1.5 L/min) prior and during
848 BLI using the XGI-8 Gas Anesthesia System. Prior to imaging, 100 µL of nanoluciferase
849 substrate, furimazine (NanoGlo^{TM}, Promega, Madison, WI) diluted 1:40 in endotoxin-
850 free PBS was retro-orbitally administered to mice under anesthesia. The mice were then
851 placed into XIC-3 animal isolation chamber (PerkinElmer) pre-saturated with isothesia
852 and oxygen mix. The mice were imaged in both dorsal and ventral position at indicated
853 days post infection. The animals were then imaged again after euthanasia and necropsy
854 by spreading additional 200 µL of substrate on to exposed intact organs. Infected areas of
855 interest identified by carrying out whole-body imaging after necropsy were isolated,
856 washed in PBS to remove residual blood and placed onto a clear plastic plate. Additional
857 droplets of furimazine in PBS (1:40) were added to organs and soaked in substrate for 1-2
858 min before BLI.

859 Images were acquired and analyzed with the manufacturer's Living Image v4.7.3
860 *in vivo* software package. Image acquisition exposures were set to auto, with imaging
861 parameter preferences set in order of exposure time, binning, and f/stop, respectively.
862 Images were acquired with luminescent f/stop of 2, photographic f/stop of 8. Binning was

863 set to medium. Comparative images were compiled and batch-processed using the image
864 browser with collective luminescent scales. Photon flux was measured as luminescent
865 radiance (p/sec/cm^2/sr). During luminescent threshold selection for image display,
866 luminescent signals were regarded as background when minimum threshold levels
867 resulted in displayed radiance above non-tissue-containing or known uninfected regions.
868 To determine the pattern of virus spread, the image sequences were acquired every day
869 following administration of SARS-CoV-2 (i.n). Image sequences were assembled and
870 converted to videos using Image J.
871
872 **Analyses of signature inflammatory cytokines mRNA**
873 Brain and lung samples were collected from mice at the time of necropsy.
874 Approximately, 20 mg of tissue was suspended in 500 µL of RLT lysis buffer, and RNA
875 was extracted using RNeasy plus Mini kit (Qiagen Cat # 74136), reverse transcribed with
876 iScript advanced cDNA kit (Bio-Rad Cat #1725036). To determine levels of signature
877 inflammatory cytokines, multiplex qPCR was conducted using iQ Multiplex Powermix
878 (Bio Rad Cat # 1725848) and PrimePCR Probe Assay mouse primers FAM-GAPDH,
879 HEX-IL6, TEX615-CCL2, Cy5-CXCL10, and Cy5.5-IFNgamma. The reaction plate was
880 analyzed using CFX96 touch real time PCR detection system. Scan mode was set to all
881 channels. The PCR conditions were 95 °C 2 min, 40 cycles of 95 °C for 10 s and 60 °C
882 for 45 s, followed by a melting curve analysis to ensure that each primer pair resulted in
883 amplification of a single PCR product. mRNA levels of il6, ccl2, cxcl10 and ifng in the
884 cDNA samples of infected mice were normalized to gapdh with the formula ΔC_t(target

gene)=C_t(target gene)-C_t(gapdh). The fold increase was determined using $2^{-\Delta\Delta Ct}$ method comparing treated mice to uninfected controls.

Protein expression and purification

FreeStyle 293F cells (Thermo Fisher) were grown in FreeStyle 293F medium (Thermo Fisher) to a density of $1x10^6$ cells/mL at 37°C with 8% CO_2 with regular agitation (135 rpm). Cells were transfected with a plasmid coding for recombinant stabilized SARS-CoV-2 ectodomain (residue 1-1208) (S-6P or HexaPro Spike; obtained from Dr. Jason S. McLellan) (Hsieh et al., 2020), his-tagged SARS-CoV-2 RBD (residue 319-541) or SARS-CoV RBD-SD1(residue 306-577) using polyethylenimine (PEI). One-week post-transfection, supernatants were clarified and filtered using a 0.22 µm filter (Thermo Fisher Scientific). The crude S-6P was purified on strep-tactin resin (IBA) followed by size-exclusion chromatography on Superose 6 10/300 column (GE Healthcare) in 10 mM Tris pH 8.0 and 200 mM NaCl (SEC buffer). RBD was purified on a Ni-NTA column (Invitrogen) followed by size-exclusion chromatography on a Hiload 16/600 Superdex 200pg column using the same SEC buffer. For CryoEM protein sample preparation, the expression plasmid encoding S-6P was transfected into 293F GnT1- cells using PEI. The protein was harvested and purified with the same protocol as above. The C-terminal twin-Strep-Tag and 8xHis tag on S-6P was removed by HRV3C (Sigma) digestion as described in (Wrapp et al., 2020b) and the cleaved protein was further purified on a Ni-NTA column followed by gel filtration on a Superose 6 10/300 in SEC buffer. Purified proteins were snap-frozen in liquid nitrogen and stored in aliquots at -80°C until further use. Protein purity was confirmed by SDS-PAGE.

908 The expression plasmids encoding the heavy and light chains of CV3-13 IgG were
909 transiently transfected into Expi293F cells (Thermo Fisher) using ExpiFectamine 293
910 transfection reagent as per the manufacturer's protocol (Thermo Fisher). After 6-days
911 post-transfection, the antibody was purified on Protein A resin from cell supernatant
912 (Thermo Fisher) before the overnight papain digestion at 37°C using immobilized papain
913 agarose (Thermo Fisher). The resulting Fab was separated from Fc and undigested IgG
914 by passage over protein A resin. Fab was further purified by gel filtration using a
915 Superose 6 10/300 column before use in SPR binding or cryo-EM sample preparation.
916 FreeStyle 293F cells (Thermo Fisher) were grown in FreeStyle 293F medium (Thermo
917 Fisher Scientific) to a density of $1x10^6$ cells/mL at 37°C with 8% CO_2 with regular
918 agitation (135 rpm). The expression plasmids encoding the heavy and light chains of
919 CV3-1, CV3-25, CV3-13 WT, CV3-13 LALA and CV3-13 GASDALIE IgG were
920 transfected into Freestyle 293F cells (Thermo Fisher Scientific) using ExpiFectamine 293
921 transfection reagent as per the manufacturer's protocol (Thermo Fisher Scientific). 1
922 week later, the cells were pelleted and discarded. The supernatants were filtered (Thermo
923 Fisher Scientific) (0.22-µm-pore-size filter) as directed by the manufacturer (Thermo
924 Fisher Scientific). The supernatant containing the antibody was then passed over Protein
925 A beads (Cytiva). Following this, the antibodies were washed, eluted and dialyzed
926 against PBS before their concentration being measured. Antibodies were then aliquoted
927 and stored at -80°C until further use.
928
929 **SARS-CoV-2 Spike ELISA (enzyme-linked immunosorbent assay)**

The SARS-CoV-2 Spike ELISA assay used was recently described (Beaudoin-Bussieres et al., 2020; Prevost et al., 2020). Briefly, recombinant SARS-CoV-2 S-6P (2.5 µg/ml), or bovine serum albumin (BSA) (2.5 µg/ml) as a negative control, were prepared in PBS and were adsorbed to plates (MaxiSorp; Nunc) overnight at 4 °C. Coated wells were subsequently blocked with blocking buffer (Tris-buffered saline [TBS] containing 0.1% Tween20 and 2% BSA) for 1 hour at room temperature. Wells were then washed four times with washing buffer (TBS containing 0.1% Tween20). CV3-1, CV3-25, CV3-13 WT, CV3-13 LALA, CV3-13 GASDALIE and CR3022 mAbs (50 ng/ml) were prepared in a diluted solution of blocking buffer (0.1 % BSA) and incubated in the coated wells for 90 minutes at room temperature. Plates were washed four times with washing buffer followed by incubation with HRP-conjugated anti-Human IgG secondary Abs (Invitrogen) (at a concentration of 0.267 µg/mL in a diluted solution of blocking buffer [0.4% BSA]) for 1 hour at room temperature, followed by four washes. HRP enzyme activity was determined after the addition of 40 µL of a 1:1 mix of Western Lightning oxidizing and luminol reagents (Perkin Elmer Life Sciences). Light emission was measured with a LB941 TriStar luminometer (Berthold Technologies). Signal obtained with BSA was subtracted for each antibody and was then normalized to the signal obtained with CR3022 mAb present in each plate.

Flow cytometry analysis of cell-surface Spike staining.

10 µg of the different expressors of the original SARS-CoV-2 Spike (Hoffmann et al., 2020) or the different mutants of the SARS-CoV-2 Spike (B.1.1.7, D614G, Δ69-70, Δ144, N501Y, A570D, P681H, T716I, S982A and D1118H) (Li et al., 2021b; Prevost et

al., 2021; Tauzin et al., 2021) were co-transfected with 2.5 µg of a green fluorescent protein (GFP) expressor (pIRES2-eGFP) into 2 × 10^6 293T cells using the standard calcium phosphate method. Before staining with primary antibodies, cells were washed 2 times. At 48 hours post transfection, 293T cells were stained with CR3022, CV3-1, CV3-13 WT, CV3-13 LALA, CV3-13 GASDALIE and CV3-25 antibodies (5µg/mL) for 45 minutes at 37°C before being washed 2 times in PBS. Alexa Fluor-647-conjugated goat anti-human IgG (H+L) Abs (Invitrogen) (2 µg/mL) and AquaVivid (Thermo Fischer Scientific) (Dilution of 1/1000) were used to stain the cells for 20 minutes at room temperature. The percentage of transfected cells (GFP+ cells) was determined by gating the living cell population based on the basis of viability dye staining (AquaVivid, Thermo Fischer Scientific). Samples were acquired on a LSRII cytometer (BD Biosciences) and data analysis was performed using FlowJo v10.5.3 (Tree Star).

For cell surface staining of transduced CEM.NKr-Spike cells, CEM.NKr-Spike cells were stained for 45 minutes at room temperature with CV3-1, CV3-13 WT, CV3-13 LALA and CV3-13 GASDALIE (0.0025 µg/mL, 0.01 µg/mL, 0.05 µg/mL, 0.25 µg/mL, 1 µg/mL and 5 µg/mL) in PBS. Cells were then washed twice with PBS and stained with 2 µg/mL of anti-human AlexaFluor 647 (AF-647) secondary antibody and 1:1000 dilution of viability dye AquaVivid (Thermo Fisher) for 20 minutes in PBS at room temperature. Cells were then washed twice with PBS and fixed in a 2% PBS-formaldehyde solution. All samples were acquired on an LSRII cytometer (BD Biosciences) and data analysis was performed using FlowJo v10.5.3 (Tree Star).

Surface plasmon resonance (SPR)

All surface plasma resonance assays were performed on a Biacore 3000 (GE Healthcare) with a running buffer of 10 mM HEPES pH 7.5 and 150 mM NaCl, supplemented with 0.05% Tween 20 at 25^{o}C. Initial epitope mapping was performed by the binding of SARS-CoV RBD (residue 306-577) and other SARS-CoV-2 antigens (S1 and S2 obtained from BEI Resources) to immobilized CV3-13 IgG (~5800 RU) on a Protein A sensor chip (Cytiva). For the kinetic measurement of CV3-13 Fab binding to SARS-CoV-2 spike, ~800 RU of his-tagged SARS-CoV-2 S-6P was immobilized on a Ni-pretreated NTA chip (Cytiva). 2-fold serial dilutions of purified CV3-13 Fab were then injected with concentrations ranging from 3.125 to 200 nM. Sensorgrams were corrected by subtraction of the corresponding blank channel as well as for the buffer background and kinetic constants determined using a 1:1 Langmuir model with the BIAevaluation software (GE Healthcare). Goodness of fit of the curve was evaluated by the Chi^2 of the fit with a value below 3 considered acceptable.

Pseudovirus neutralization assay

Target cells were infected with single-round luciferase-expressing lentiviral particles. Briefly, 293T cells were transfected by the calcium phosphate method with the pNL4.3 R-E- Luc plasmid (NIH AIDS Reagent Program) and a plasmid encoding for SARS-CoV-2 Spike at a ratio of 10:1. Two days post-transfection, cell supernatants were harvested and stored at –80°C until use. 293T-ACE2 (Prevost et al., 2020) target cells were seeded at a density of 1×10^4 cells/well in 96-well luminometer-compatible tissue culture plates (Perkin Elmer) 24 h before infection. Recombinant viruses in a final volume of 100 µL were incubated with the indicated semi-log diluted antibody

concentrations (0 µg/mL, 0.01 µg/mL, 0.0316 µg/mL, 0.1 µg/mL, 0.316 µg/mL, 1 µg/mL, 3.16 µg/mL and 10 µg/mL) for 1 h at 37°C and were then added to the target cells followed by incubation for 48 h at 37°C; cells were lysed by the addition of 30 µL of passive lysis buffer (Promega) followed by one freeze-thaw cycle. An LB941 TriStar luminometer (Berthold Technologies) was used to measure the luciferase activity of each well after the addition of 100 µL of luciferin buffer (15 mM $MgSO_4$, 15 mM KH_2PO_4 [pH 7.8], 1 mM ATP, and 1 mM dithiothreitol) and 50 µL of 1 mM d-luciferin potassium salt.

Microneutralization assay

One day prior to infection, $2x10^4$ Vero E6 cells were seeded per well of a 96 well flat bottom plate and incubated overnight to permit Vero E6 cell adherence. Antibody concentrations (0 µg/mL, 0.01 µg/mL, 0.0316 µg/mL, 0.1 µg/mL, 0.316 µg/mL, 1 µg/mL, 3.16 µg/mL and 10 µg/mL) were performed in a separate 96 well culture plate using DMEM supplemented with penicillin (100 U/mL), streptomycin (100 µg/mL), HEPES, 0.12% sodium bicarbonate, 2% FBS and 0.24% BSA. 10^4 $TCID_{50}$/mL of authentic SARS-CoV-2 D614G virus (derived from strain LSPQ/231457/2020; (Prevost et al., 2021)) was prepared in DMEM + 2% FBS and combined with an equivalent volume of diluted antibodies for one hour. After this incubation, all media was removed from the 96 well plate seeded with Vero E6 cells and virus:antibody mixture was added to each respective well at a volume corresponding to 600 $TCID_{50}$ per well and incubated for one hour further at 37°C. Both virus only and media only (MEM + 2% FBS) conditions were included in this assay. All virus:antibody supernatant was removed from

wells without disrupting the Vero E6 monolayer. Each diluted antibody (for a volume of 100 µL) was added to its respective Vero E6-seeded well in addition to an equivalent volume of MEM + 2% FBS and was then incubated for 48 hours. Media was then discarded and replaced with 10% formaldehyde for 24 hours to cross-link Vero E6 monolayer. After, formaldehyde was removed from wells and subsequently washed with PBS. Cell monolayers were permeabilized for 15 minutes at room temperature with PBS + 0.1% Triton X-100, washed with PBS and then incubated for one hour at room temperature with PBS + 3% non-fat milk. A mouse anti-SARS-CoV-2 nucleocapsid protein monoclonal antibody (Clone 1C7, Bioss Antibodies) solution was prepared at 1 µg/mL in PBS + 1% non-fat milk and added to all wells for one hour at room temperature. Following extensive washing (3×) with PBS, an anti-mouse IgG HRP secondary antibody solution was formulated in PBS + 1% non-fat milk. One hour post-room temperature incubation, wells were washed with 3×PBS, substrate (ECL) was added and an LB941 TriStar luminometer (Berthold Technologies) was used to measure the signal each well.

Cell-surface staining of SARS-CoV-2-infected cells

8M Vero-E6 cells were plated in T-175 flask 24 hours before infection. Authentic SARS-CoV-2 virus (MOI = 0.01) was used for infection. After 48 hours, infected Vero E6 cells were detached with PBS-EDTA and were incubated with 5 µg/mL of indicated antibodies for 30 minutes at 37℃, followed by staining with anti-human –AF647 secondary antibody and 1:1000 dilution of viability dye AquaVivid (Thermo Fisher Scientific) for 20 minutes at room temperature. Cells were then treated with 4% PFA for 24 hours at

4℃. Then the cells were stained intracellularly for SARS-CoV-2 nucleocapsid (N) antigen, using the Cytofix/Cytoperm fixation/permeabilization kit (BD Biosciences) and an anti-N mAb (clone mBG17; Kerafast) conjugated with the Alexa Fluor 488 dye according to the manufacturer's instructions (Invitrogen). The percentage of infected cells (N+ cells) was determined by gating the living cell population based on the basis of viability dye staining (Aqua Vivid, Invitrogen). Samples were acquired on a LSRII cytometer (BD Biosciences, Mississauga, ON, Canada) and data analysis was performed using FlowJo v10.5.3 (Tree Star, Ashland, OR, USA).

Antibody dependent cellular cytotoxicity (ADCC) assay

This assay was previously described (Anand et al., 2021). Briefly, for evaluation of anti-SARS-CoV-2 ADCC activity, parental CEM.NKr CCR5+ cells were mixed at a 1:1 ratio with CEM.NKr-Spike cells. These cells were stained for viability (AquaVivid; Thermo Fisher Scientific) and a cellular dye (cell proliferation dye eFluor670; Thermo Fisher Scientific) and subsequently used as target cells. Overnight rested PBMCs were stained with another cellular marker (cell proliferation dye eFluor450; Thermo Fisher Scientific) and used as effector cells. Stained effector and target cells were mixed at a 10:1 ratio in 96-well V-bottom plates. Titrated concentrations of CV3-1, CV3-13 WT, CV3-13 LALA and CV3-13 GASDALIE monoclonal antibodies (0.0025 µg/mL, 0.01 µg/mL, 0.05 µg/mL, 0.25 µg/mL, 1 µg/mL and 5 µg/mL) were added to the appropriate wells. The plates were subsequently centrifuged for 1 min at 300 x g, and incubated at 37°C, 5% CO_2 for 5 hours before being fixed in a 2% PBS-formaldehyde solution. Since CEM.NKr-Spike cells express GFP, ADCC activity was calculated using the formula:

[(% of GFP+ cells in Targets plus Effectors) - (% of GFP+ cells in Targets plus Effectors plus antibody)] / (% of GFP+ cells in Targets) x 100 by gating on transduced live target cells. All samples were acquired on an LSRII cytometer (BD Biosciences) and data analysis performed using FlowJo v10.5.3 (Tree Star).

Antibody dependent cellular phagocytosis (ADCP) assay

The ADCP assay was performed using CEM.NKr-Spike cells as target cells that were fluorescently labelled with a cellular dye (cell proliferation dye eFluor450). THP-1 cells were used as effector cells and were stained with another cellular dye (cell proliferation dye eFluor670). Stained target cells were incubated with 100 µL of the titrated concentrations of CV3-1, CV3-13 WT, CV3-13 LALA and CV3-13 GASDALIE antibodies (0,625 µg/mL, 1,25 µg/mL, 2,5 µg/mL, 5 µg/mL and 10 µg/mL) for 1h at 37°C, followed by two washes with media. Stained target and effector cells were mixed at a 5:1 ratio in 96-well U-bottom plates. After a 5 hours incubation at 37 °C and 5% CO_2, cells were fixed with a 2% PBS-formaldehyde solution. Antibody-mediated phagocytosis was determined by flow cytometry, gating on THP-1 cells that were triple-positive for eFluor450 and eFluor670 cellular dyes and GFP. All samples were acquired on an LSRII cytometer (BD Biosciences) and data analysis performed using FlowJo v10.5.3 (Tree Star).

Cryo-EM sample preparation and data collection

SARS-CoV-2 HexaPro spike (GnT1- produced) was incubated with 20-fold excess of CV3-13 Fab overnight at 4°C before purification on a Superose 6 300/10 GL column (GE

Healthcare). The complex peak was harvested, concentrated to 0.50 mg/mL in the SEC buffer and immediately used for Cryo-EM grid preparation. 3µL of protein was deposited on a holey copper grids (QUANTIFOIL R 1.2/1.3, 200 mesh, EMS) which had been glow-discharged for 30s at 15 Ma using PELCO easiGlow (TedPella Inc). Grids were vitrified in liquid ethane using Vitrobot Mark IV (Thermo Fisher) with a blot time of 2-4 s and variable blot force at 4^{o}C and 100% humidity.

The frozen grids were screened on a FEI Talos Arctica microscope at 200 kV equipped with a FEI Falcon3EC detector using the EPU software (Thermo Fisher). Cryo-EM data from a good grid were acquired on a FEI Glacios electron microscope operating at 200 kV, equipped with a Gatan K3 direct electron detector. Micrographs were collected at a magnification of 45,000 corresponding to a calibrated pixel size of 0.8893 Å, with a total exposure dose of 42 e-/ Å^{2}.

Cryo-EM data processing, model building and analysis

Motion correction, CTF estimation, particle picking, curation and extraction, 2D classification, *ab initio* model reconstruction, volume refinements and local resolution estimation were carried out in cryoSPARC (Punjani et al., 2017; Rubinstein and Brubaker, 2015). An initial SARS-CoV-2 spike model (PDB: 6XKL) with single-RBD up and a three-RBD-down (closed) model (PDB: 6VXX) were used as modeling templates. The NTDs were initially modelled from PDB entry 7C2L. The initial models for CV3-13 Fab were generated in the SAbPred server (Dunbar et al., 2016) using the primary sequence.

Automated and manual model refinements were iteratively carried out in ccpEM (Burnley et al., 2017), Phenix (Liebschner et al., 2019) (real-space refinement) and Coot (Emsley and Cowtan, 2004). Geometry validation and structure quality evaluation were performed by EM-Ringer (Barad et al., 2015) and Molprobity (Chen et al., 2010). Model-to-map fitting cross correlation and figures generation were carried out in USCF Chimera, Chimera X (Pettersen et al., 2021) and PyMOL (The PyMOL Molecular Graphics System, Version 1.2r3pre, Schrödinger, LLC). The complete cryo-EM data processing workflow is shown in Figure S4 and statistics of data collection, reconstruction and refinement is described in Table S1. The epitope interface analysis was performed in PISA (Krissinel and Henrick, 2007).

Quantification and Statistical Analysis

Statistical significance was derived by applying parametric unpaired t-test or non-parametric Mann-Whitney U test (two-tailed) available in GraphPad Prism software (La Jolla, CA, USA) depending on the normality distribution of the data. *p* values lower than 0.05 were considered statistically significant. P values were indicated as $*$, $p < 0.05$; $**$, $p < 0.01$; $***$, $p < 0.001$; $****$, $p < 0.0001$.

References

Adeniji, O.S., Giron, L.B., Purwar, M., Zilberstein, N.F., Kulkarni, A.J., Shaikh, M.W., Balk, R.A., Moy, J.N., Forsyth, C.B., Liu, Q., *et al.* (2021). COVID-19 Severity Is Associated with Differential Antibody Fc-Mediated Innate Immune Functions. mBio *12*.

Alter, G., Gorman, M., Patel, N., Guebre-Xabier, M., Zhu, A., Atyeo, C., Pullen, K., Loos, C., Goez-Gazi, Y., Carrion, R., *et al.* (2021). Collaboration between the Fab and Fc contribute to maximal protection against SARS-CoV-2 following NVX-CoV2373 subunit vaccine with Matrix-M vaccination. Res Sq.

Amanat, F., Thapa, M., Lei, T., Ahmed, S.M.S., Adelsberg, D.C., Carreno, J.M., Strohmeier, S., Schmitz, A.J., Zafar, S., Zhou, J.Q., *et al.* (2021). The plasmablast response to SARS-CoV-2 mRNA vaccination is dominated by non-neutralizing antibodies that target both the NTD and the RBD. medRxiv.

Amraie, R., Napoleon, M.A., Yin, W., Berrigan, J., Suder, E., Zhao, G., Olejnik, J., Gummuluru, S., Muhlberger, E., Chitalia, V., *et al.* (2020). CD209L/L-SIGN and CD209/DC-SIGN act as receptors for SARS-CoV-2 and are differentially expressed in lung and kidney epithelial and endothelial cells. bioRxiv.

Anand, S.P., Prevost, J., Nayrac, M., Beaudoin-Bussieres, G., Benlarbi, M., Gasser, R., Brassard, N., Laumaea, A., Gong, S.Y., Bourassa, C., *et al.* (2021). Longitudinal analysis of humoral immunity against SARS-CoV-2 Spike in convalescent individuals up to 8 months post-symptom onset. Cell Rep Med *2*, 100290.

AstraZeneca, and Iqvia Pty, L. (2021). Phase III Double-blind, Placebo-controlled Study of AZD1222 for the Prevention of COVID-19 in Adults.

Baden, L.R., El Sahly, H.M., Essink, B., Kotloff, K., Frey, S., Novak, R., Diemert, D., Spector, S.A., Rouphael, N., Creech, C.B., *et al.* (2021). Efficacy and Safety of the mRNA-1273 SARS-CoV-2 Vaccine. N Engl J Med *384*, 403-416.

Barad, B.A., Echols, N., Wang, R.Y., Cheng, Y., DiMaio, F., Adams, P.D., and Fraser, J.S. (2015). EMRinger: side chain-directed model and map validation for 3D cryo-electron microscopy. Nat Methods *12*, 943-946.

Beaudoin-Bussieres, G., Laumaea, A., Anand, S.P., Prevost, J., Gasser, R., Goyette, G., Medjahed, H., Perreault, J., Tremblay, T., Lewin, A., *et al.* (2020). Decline of Humoral Responses against SARS-CoV-2 Spike in Convalescent Individuals. mBio *11*.

Bio, N.S.E., and Pfizer (2021). Study to Describe the Safety, Tolerability, Immunogenicity, and Efficacy of RNA Vaccine Candidates Against COVID-19 in Healthy Individuals.

Bournazos, S., Klein, F., Pietzsch, J., Seaman, M.S., Nussenzweig, M.C., and Ravetch, J.V. (2014). Broadly neutralizing anti-HIV-1 antibodies require Fc effector functions for in vivo activity. Cell *158*, 1243-1253.

Brunet-Ratnasingham, E., Anand, S.P., Gantner, P., Moquin-Beaudry, G., Dyachenko, A., Brassard, N., Beaudoin-Bussières, G., Pagliuzza, A., Gasser, R., Benlarbi, M., *et al.* (2021). Integrated immunovirological profiling validates plasma SARS-CoV-2 RNA as an early predictor of COVID-19 mortality. 2021.2003.2018.21253907.

Buchrieser, J., Dufloo, J., Hubert, M., Monel, B., Planas, D., Rajah, M.M., Planchais, C., Porrot, F., Guivel-Benhassine, F., Van der Werf, S., *et al.* (2020). Syncytia formation by SARS-CoV-2-infected cells. EMBO J *39*, e106267.

Burnley, T., Palmer, C.M., and Winn, M. (2017). Recent developments in the CCP-EM software suite. Acta Crystallogr D Struct Biol *73*, 469-477.

1178 Cao, Y., Su, B., Guo, X., Sun, W., Deng, Y., Bao, L., Zhu, Q., Zhang, X., Zheng, Y.,
1179 Geng, C., *et al.* (2020). Potent Neutralizing Antibodies against SARS-CoV-2 Identified
1180 by High-Throughput Single-Cell Sequencing of Convalescent Patients' B Cells. Cell *182*,
1181 73-84 e16.
1182 Cerutti, G., Guo, Y., Zhou, T., Gorman, J., Lee, M., Rapp, M., Reddem, E.R., Yu, J.,
1183 Bahna, F., Bimela, J., *et al.* (2021). Potent SARS-CoV-2 neutralizing antibodies directed
1184 against spike N-terminal domain target a single supersite. Cell Host Microbe *29*, 819-833
1185 e817.
1186 Chen, V.B., Arendall, W.B., 3rd, Headd, J.J., Keedy, D.A., Immormino, R.M., Kapral,
1187 G.J., Murray, L.W., Richardson, J.S., and Richardson, D.C. (2010). MolProbity: all-atom
1188 structure validation for macromolecular crystallography. Acta Crystallogr D Biol
1189 Crystallogr *66*, 12-21.
1190 Chen, X., Li, R., Pan, Z., Qian, C., Yang, Y., You, R., Zhao, J., Liu, P., Gao, L., Li, Z., *et*
1191 *al.* (2020). Human monoclonal antibodies block the binding of SARS-CoV-2 spike
1192 protein to angiotensin converting enzyme 2 receptor. Cell Mol Immunol *17*, 647-649.
1193 Chi, X., Yan, R., Zhang, J., Zhang, G., Zhang, Y., Hao, M., Zhang, Z., Fan, P., Dong, Y.,
1194 Yang, Y., *et al.* (2020). A neutralizing human antibody binds to the N-terminal domain of
1195 the Spike protein of SARS-CoV-2. Science *369*, 650-655.
1196 DiLillo, D.J., and Ravetch, J.V. (2015). Differential Fc-Receptor Engagement Drives an
1197 Anti-tumor Vaccinal Effect. Cell *161*, 1035-1045.
1198 Duan, L., Zheng, Q., Zhang, H., Niu, Y., Lou, Y., and Wang, H. (2020). The SARS-CoV-
1199 2 Spike Glycoprotein Biosynthesis, Structure, Function, and Antigenicity: Implications
1200 for the Design of Spike-Based Vaccine Immunogens. Front Immunol *11*, 576622.
1201 Dunbar, J., Krawczyk, K., Leem, J., Marks, C., Nowak, J., Regep, C., Georges, G., Kelm,
1202 S., Popovic, B., and Deane, C.M. (2016). SAbPred: a structure-based antibody prediction
1203 server. Nucleic Acids Res *44*, W474-478.
1204 Durocher, Y., Perret, S., and Kamen, A. (2002). High-level and high-throughput
1205 recombinant protein production by transient transfection of suspension-growing human
1206 293-EBNA1 cells. Nucleic Acids Res *30*, E9.
1207 Emary, K.R.W., Golubchik, T., Aley, P.K., Ariani, C.V., Angus, B., Bibi, S., Blane, B.,
1208 Bonsall, D., Cicconi, P., Charlton, S., *et al.* (2021). Efficacy of ChAdOx1 nCoV-19
1209 (AZD1222) vaccine against SARS-CoV-2 variant of concern 202012/01 (B.1.1.7): an
1210 exploratory analysis of a randomised controlled trial. Lancet *397*, 1351-1362.
1211 Emsley, P., and Cowtan, K. (2004). Coot: model-building tools for molecular graphics.
1212 Acta Crystallogr D Biol Crystallogr *60*, 2126-2132.
1213 Emsley, P., Lohkamp, B., Scott, W.G., and Cowtan, K. (2010). Features and development
1214 of Coot. Acta Crystallogr D Biol Crystallogr *66*, 486-501.
1215 Gasser, R., Cloutier, M., Prevost, J., Fink, C., Ducas, E., Ding, S., Dussault, N., Landry,
1216 P., Tremblay, T., Laforce-Lavoie, A., *et al.* (2021). Major role of IgM in the neutralizing
1217 activity of convalescent plasma against SARS-CoV-2. Cell Rep *34*, 108790.
1218 Goddard, T.D., Huang, C.C., and Ferrin, T.E. (2007). Visualizing density maps with
1219 UCSF Chimera. J Struct Biol *157*, 281-287.
1220 Goddard, T.D., Huang, C.C., Meng, E.C., Pettersen, E.F., Couch, G.S., Morris, J.H., and
1221 Ferrin, T.E. (2018). UCSF ChimeraX: Meeting modern challenges in visualization and
1222 analysis. Protein Sci *27*, 14-25.

Harvey, W.T., Carabelli, A.M., Jackson, B., Gupta, R.K., Thomson, E.C., Harrison, E.M., Ludden, C., Reeve, R., Rambaut, A., Consortium, C.-G.U., *et al.* (2021). SARS-CoV-2 variants, spike mutations and immune escape. Nat Rev Microbiol *19*, 409-424.

Hoffmann, M., Kleine-Weber, H., Schroeder, S., Kruger, N., Herrler, T., Erichsen, S., Schiergens, T.S., Herrler, G., Wu, N.H., Nitsche, A., *et al.* (2020). SARS-CoV-2 Cell Entry Depends on ACE2 and TMPRSS2 and Is Blocked by a Clinically Proven Protease Inhibitor. Cell *181*, 271-280 e278.

Hsieh, C.L., Goldsmith, J.A., Schaub, J.M., DiVenere, A.M., Kuo, H.C., Javanmardi, K., Le, K.C., Wrapp, D., Lee, A.G., Liu, Y., *et al.* (2020). Structure-based design of prefusion-stabilized SARS-CoV-2 spikes. Science *369*, 1501-1505.

Huang, C., Wang, Y., Li, X., Ren, L., Zhao, J., Hu, Y., Zhang, L., Fan, G., Xu, J., Gu, X., *et al.* (2020). Clinical features of patients infected with 2019 novel coronavirus in Wuhan, China. Lancet *395*, 497-506.

Hurlburt, N.K., Seydoux, E., Wan, Y.H., Edara, V.V., Stuart, A.B., Feng, J., Suthar, M.S., McGuire, A.T., Stamatatos, L., and Pancera, M. (2020). Structural basis for potent neutralization of SARS-CoV-2 and role of antibody affinity maturation. Nat Commun *11*, 5413.

Janssen, V., and Prevention, B.V. (2021). A Study of Ad26.COV2.S for the Prevention of SARS-CoV-2-Mediated COVID-19 in Adult Participants.

Jennewein, M.F., MacCamy, A.J., Akins, N.R., Feng, J., Homad, L.J., Hurlburt, N.K., Seydoux, E., Wan, Y.H., Stuart, A.B., Edara, V.V., *et al.* (2021). Isolation and characterization of cross-neutralizing coronavirus antibodies from COVID-19+ subjects. Cell Rep, 109353.

Ju, B., Zhang, Q., Ge, J., Wang, R., Sun, J., Ge, X., Yu, J., Shan, S., Zhou, B., Song, S., *et al.* (2020). Human neutralizing antibodies elicited by SARS-CoV-2 infection. Nature *584*, 115-119.

Krissinel, E., and Henrick, K. (2007). Inference of macromolecular assemblies from crystalline state. J Mol Biol *372*, 774-797.

Ksiazek, T.G., Erdman, D., Goldsmith, C.S., Zaki, S.R., Peret, T., Emery, S., Tong, S., Urbani, C., Comer, J.A., Lim, W., *et al.* (2003). A novel coronavirus associated with severe acute respiratory syndrome. N Engl J Med *348*, 1953-1966.

Lan, J., Ge, J., Yu, J., Shan, S., Zhou, H., Fan, S., Zhang, Q., Shi, X., Wang, Q., Zhang, L., *et al.* (2020). Structure of the SARS-CoV-2 spike receptor-binding domain bound to the ACE2 receptor. Nature *581*, 215-220.

Lazar, G.A., Dang, W., Karki, S., Vafa, O., Peng, J.S., Hyun, L., Chan, C., Chung, H.S., Eivazi, A., Yoder, S.C., *et al.* (2006). Engineered antibody Fc variants with enhanced effector function. Proc Natl Acad Sci U S A *103*, 4005-4010.

Lempp, F.A., Soriaga, L., Montiel-Ruiz, M., Benigni, F., Noack, J., Park, Y.-J., Bianchi, S., Walls, A.C., Bowen, J.E., Zhou, J., *et al.* (2021). Membrane lectins enhance SARS-CoV-2 infection and influence the neutralizing activity of different classes of antibodies. 2021.2004.2003.438258.

Li, D., Edwards, R.J., Manne, K., Martinez, D.R., Schafer, A., Alam, S.M., Wiehe, K., Lu, X., Parks, R., Sutherland, L.L., *et al.* (2021a). In vitro and in vivo functions of SARS-CoV-2 infection-enhancing and neutralizing antibodies. Cell *184*, 4203-4219 e4232.

Li, W., Chen, Y., Prevost, J., Ullah, I., Lu, M., Gong, S.Y., Tauzin, A., Gasser, R., Vezina, D., Anand, S.P., *et al.* (2021b). Structural Basis and Mode of Action for Two

Broadly Neutralizing Antibodies Against SARS-CoV-2 Emerging Variants of Concern. bioRxiv.

Liebschner, D., Afonine, P.V., Baker, M.L., Bunkoczi, G., Chen, V.B., Croll, T.I., Hintze, B., Hung, L.W., Jain, S., McCoy, A.J., *et al.* (2019). Macromolecular structure determination using X-rays, neutrons and electrons: recent developments in Phenix. Acta Crystallogr D Struct Biol *75*, 861-877.

Liu, L., Wang, P., Nair, M.S., Yu, J., Rapp, M., Wang, Q., Luo, Y., Chan, J.F., Sahi, V., Figueroa, A., *et al.* (2020). Potent neutralizing antibodies against multiple epitopes on SARS-CoV-2 spike. Nature *584*, 450-456.

Liu, Y., Soh, W.T., Kishikawa, J.I., Hirose, M., Nakayama, E.E., Li, S., Sasai, M., Suzuki, T., Tada, A., Arakawa, A., *et al.* (2021). An infectivity-enhancing site on the SARS-CoV-2 spike protein targeted by antibodies. Cell *184*, 3452-3466 e3418.

Long, Q.X., Tang, X.J., Shi, Q.L., Li, Q., Deng, H.J., Yuan, J., Hu, J.L., Xu, W., Zhang, Y., Lv, F.J., *et al.* (2020). Clinical and immunological assessment of asymptomatic SARS-CoV-2 infections. Nat Med *26*, 1200-1204.

Lu, M., Uchil, P.D., Li, W., Zheng, D., Terry, D.S., Gorman, J., Shi, W., Zhang, B., Zhou, T., Ding, S., *et al.* (2020). Real-Time Conformational Dynamics of SARS-CoV-2 Spikes on Virus Particles. Cell Host Microbe *28*, 880-891 e888.

Luchsinger, L.L., Ransegnola, B.P., Jin, D.K., Muecksch, F., Weisblum, Y., Bao, W., George, P.J., Rodriguez, M., Tricoche, N., Schmidt, F., *et al.* (2020). Serological Assays Estimate Highly Variable SARS-CoV-2 Neutralizing Antibody Activity in Recovered COVID-19 Patients. J Clin Microbiol *58*.

McCallum, M., De Marco, A., Lempp, F.A., Tortorici, M.A., Pinto, D., Walls, A.C., Beltramello, M., Chen, A., Liu, Z., Zatta, F., *et al.* (2021). N-terminal domain antigenic mapping reveals a site of vulnerability for SARS-CoV-2. Cell *184*, 2332-2347 e2316.

McCarthy, K.R., Rennick, L.J., Nambulli, S., Robinson-McCarthy, L.R., Bain, W.G., Haidar, G., and Duprex, W.P. (2021). Recurrent deletions in the SARS-CoV-2 spike glycoprotein drive antibody escape. Science *371*, 1139-1142.

ModernaTx, I., Biomedical Advanced, R., Development, A., National Institute of, A., and Infectious, D. (2022). A Study to Evaluate Efficacy, Safety, and Immunogenicity of mRNA-1273 Vaccine in Adults Aged 18 Years and Older to Prevent COVID-19.

Muecksch, F., Wise, H., Batchelor, B., Squires, M., Semple, E., Richardson, C., McGuire, J., Clearly, S., Furrie, E., Greig, N., *et al.* (2021). Longitudinal Serological Analysis and Neutralizing Antibody Levels in Coronavirus Disease 2019 Convalescent Patients. J Infect Dis *223*, 389-398.

Oliver, S.E., Gargano, J.W., Marin, M., Wallace, M., Curran, K.G., Chamberland, M., McClung, N., Campos-Outcalt, D., Morgan, R.L., Mbaeyi, S., *et al.* (2021a). The Advisory Committee on Immunization Practices' Interim Recommendation for Use of Moderna COVID-19 Vaccine - United States, December 2020. MMWR Morb Mortal Wkly Rep *69*, 1653-1656.

Oliver, S.E., Gargano, J.W., Scobie, H., Wallace, M., Hadler, S.C., Leung, J., Blain, A.E., McClung, N., Campos-Outcalt, D., Morgan, R.L., *et al.* (2021b). The Advisory Committee on Immunization Practices' Interim Recommendation for Use of Janssen COVID-19 Vaccine - United States, February 2021. MMWR Morb Mortal Wkly Rep *70*, 329-332.

Payne, D.C., Smith-Jeffcoat, S.E., Nowak, G., Chukwuma, U., Geibe, J.R., Hawkins, R.J., Johnson, J.A., Thornburg, N.J., Schiffer, J., Weiner, Z., *et al.* (2020). SARS-CoV-2 Infections and Serologic Responses from a Sample of U.S. Navy Service Members - USS Theodore Roosevelt, April 2020. MMWR Morb Mortal Wkly Rep *69*, 714-721.

Pettersen, E.F., Goddard, T.D., Huang, C.C., Meng, E.C., Couch, G.S., Croll, T.I., Morris, J.H., and Ferrin, T.E. (2021). UCSF ChimeraX: Structure visualization for researchers, educators, and developers. Protein Sci *30*, 70-82.

Pfizer/BioNTech (2021). Pfizer and BioNTech Confirm High Efficacy and No Serious Safety Concerns Through Up to Six Months Following Second Dose in Updated Topline Analysis of Landmark COVID-19 Vaccine Study.

Piccoli, L., Park, Y.J., Tortorici, M.A., Czudnochowski, N., Walls, A.C., Beltramello, M., Silacci-Fregni, C., Pinto, D., Rosen, L.E., Bowen, J.E., *et al.* (2020). Mapping Neutralizing and Immunodominant Sites on the SARS-CoV-2 Spike Receptor-Binding Domain by Structure-Guided High-Resolution Serology. Cell *183*, 1024-1042 e1021.

Polack, F.P., Thomas, S.J., Kitchin, N., Absalon, J., Gurtman, A., Lockhart, S., Perez, J.L., Perez Marc, G., Moreira, E.D., Zerbini, C., *et al.* (2020). Safety and Efficacy of the BNT162b2 mRNA Covid-19 Vaccine. N Engl J Med *383*, 2603-2615.

Prevost, J., Gasser, R., Beaudoin-Bussieres, G., Richard, J., Duerr, R., Laumaea, A., Anand, S.P., Goyette, G., Benlarbi, M., Ding, S., *et al.* (2020). Cross-Sectional Evaluation of Humoral Responses against SARS-CoV-2 Spike. Cell Rep Med *1*, 100126.

Prevost, J., Richard, J., Gasser, R., Ding, S., Fage, C., Anand, S.P., Adam, D., Vergara, N.G., Tauzin, A., Benlarbi, M., *et al.* (2021). Impact of temperature on the affinity of SARS-CoV-2 Spike for ACE2. bioRxiv.

Punjani, A., Rubinstein, J.L., Fleet, D.J., and Brubaker, M.A. (2017). cryoSPARC: algorithms for rapid unsupervised cryo-EM structure determination. Nat Methods *14*, 290-296.

Rappazzo, C.G., Tse, L.V., Kaku, C.I., Wrapp, D., Sakharkar, M., Huang, D., Deveau, L.M., Yockachonis, T.J., Herbert, A.S., Battles, M.B., *et al.* (2021). Broad and potent activity against SARS-like viruses by an engineered human monoclonal antibody. Science *371*, 823-829.

Richards, J.O., Karki, S., Lazar, G.A., Chen, H., Dang, W., and Desjarlais, J.R. (2008). Optimization of antibody binding to FcgammaRIIa enhances macrophage phagocytosis of tumor cells. Mol Cancer Ther *7*, 2517-2527.

Robbiani, D.F., Gaebler, C., Muecksch, F., Lorenzi, J.C.C., Wang, Z., Cho, A., Agudelo, M., Barnes, C.O., Gazumyan, A., Finkin, S., *et al.* (2020). Convergent antibody responses to SARS-CoV-2 in convalescent individuals. Nature *584*, 437-442.

Rubinstein, J.L., and Brubaker, M.A. (2015). Alignment of cryo-EM movies of individual particles by optimization of image translations. J Struct Biol *192*, 188-195.

Saunders, K.O. (2019). Conceptual Approaches to Modulating Antibody Effector Functions and Circulation Half-Life. Front Immunol *10*, 1296.

Schafer, A., Muecksch, F., Lorenzi, J.C.C., Leist, S.R., Cipolla, M., Bournazos, S., Schmidt, F., Maison, R.M., Gazumyan, A., Martinez, D.R., *et al.* (2021). Antibody potency, effector function, and combinations in protection and therapy for SARS-CoV-2 infection in vivo. J Exp Med *218*.

Scheres, S.H., and Chen, S. (2012). Prevention of overfitting in cryo-EM structure determination. Nat Methods *9*, 853-854.

Seydoux, E., Homad, L.J., MacCamy, A.J., Parks, K.R., Hurlburt, N.K., Jennewein, M.F., Akins, N.R., Stuart, A.B., Wan, Y.H., Feng, J., *et al.* (2020). Analysis of a SARS-CoV-2-Infected Individual Reveals Development of Potent Neutralizing Antibodies with Limited Somatic Mutation. Immunity *53*, 98-105 e105.

Shang, J., Wan, Y., Luo, C., Ye, G., Geng, Q., Auerbach, A., and Li, F. (2020). Cell entry mechanisms of SARS-CoV-2. Proc Natl Acad Sci U S A *117*, 11727-11734.

Skowronski, D.M., and De Serres, G. (2021). Safety and Efficacy of the BNT162b2 mRNA Covid-19 Vaccine. N Engl J Med *384*.

Smith, P., DiLillo, D.J., Bournazos, S., Li, F., and Ravetch, J.V. (2012). Mouse model recapitulating human Fcgamma receptor structural and functional diversity. Proc Natl Acad Sci U S A *109*, 6181-6186.

Soh, W.T., Liu, Y., Nakayama, E.E., Ono, C., Torii, S., Nakagami, H., Matsuura, Y., Shioda, T., and Arase, H. (2020). The N-terminal domain of spike glycoprotein mediates SARS-CoV-2 infection by associating with L-SIGN and DC-SIGN. 2020.2011.2005.369264.

Stankov, M.V., Cossmann, A., Bonifacius, A., Dopfer-Jablonka, A., Ramos, G.M., Gödecke, N., Scharff, A.Z., Happle, C., Boeck, A.-L., Tran, A.T., *et al.* (2021). Humoral and cellular immune responses against SARS-CoV-2 variants and human coronaviruses after single BNT162b2 vaccination. 2021.2004.2016.21255412.

Sun, Y., Wang, L., Feng, R., Wang, N., Wang, Y., Zhu, D., Xing, X., Yang, P., Zhang, Y., Li, W., *et al.* (2021). Structure-based development of three- and four-antibody cocktails against SARS-CoV-2 via multiple mechanisms. Cell Res *31*, 597-600.

Suryadevara, N., Shrihari, S., Gilchuk, P., VanBlargan, L.A., Binshtein, E., Zost, S.J., Nargi, R.S., Sutton, R.E., Winkler, E.S., Chen, E.C., *et al.* (2021). Neutralizing and protective human monoclonal antibodies recognizing the N-terminal domain of the SARS-CoV-2 spike protein. Cell *184*, 2316-2331 e2315.

Tauzin, A., Nayrac, M., Benlarbi, M., Gong, S.Y., Gasser, R., Beaudoin-Bussieres, G., Brassard, N., Laumaea, A., Vezina, D., Prevost, J., *et al.* (2021). A single dose of the SARS-CoV-2 vaccine BNT162b2 elicits Fc-mediated antibody effector functions and T cell responses. Cell Host Microbe.

ter Meulen, J., van den Brink, E.N., Poon, L.L., Marissen, W.E., Leung, C.S., Cox, F., Cheung, C.Y., Bakker, A.Q., Bogaards, J.A., van Deventer, E., *et al.* (2006). Human monoclonal antibody combination against SARS coronavirus: synergy and coverage of escape mutants. PLoS Med *3*, e237.

Tian, X., Li, C., Huang, A., Xia, S., Lu, S., Shi, Z., Lu, L., Jiang, S., Yang, Z., Wu, Y., *et al.* (2020). Potent binding of 2019 novel coronavirus spike protein by a SARS coronavirus-specific human monoclonal antibody. Emerg Microbes Infect *9*, 382-385.

Tortorici, M.A., Beltramello, M., Lempp, F.A., Pinto, D., Dang, H.V., Rosen, L.E., McCallum, M., Bowen, J., Minola, A., Jaconi, S., *et al.* (2020). Ultrapotent human antibodies protect against SARS-CoV-2 challenge via multiple mechanisms. Science *370*, 950-957.

Ullah, I., Prevost, J., Ladinsky, M.S., Stone, H., Lu, M., Anand, S.P., Beaudoin-Bussieres, G., Symmes, K., Benlarbi, M., Ding, S., *et al.* (2021). Live Imaging of SARS-CoV-2 Infection in Mice Reveals Neutralizing Antibodies Require Fc Function for Optimal Efficacy. bioRxiv.

1405 Voss, W.N., Hou, Y.J., Johnson, N.V., Delidakis, G., Kim, J.E., Javanmardi, K., Horton,
1406 A.P., Bartzoka, F., Paresi, C.J., Tanno, Y., *et al.* (2021). Prevalent, protective, and
1407 convergent IgG recognition of SARS-CoV-2 non-RBD spike epitopes. Science *372*,
1408 1108-1112.
1409 Voysey, M., Clemens, S.A.C., Madhi, S.A., Weckx, L.Y., Folegatti, P.M., Aley, P.K.,
1410 Angus, B., Baillie, V.L., Barnabas, S.L., Bhorat, Q.E., *et al.* (2021). Safety and efficacy
1411 of the ChAdOx1 nCoV-19 vaccine (AZD1222) against SARS-CoV-2: an interim analysis
1412 of four randomised controlled trials in Brazil, South Africa, and the UK. Lancet *397*, 99-
1413 111.
1414 Walls, A.C., Park, Y.J., Tortorici, M.A., Wall, A., McGuire, A.T., and Veesler, D.
1415 (2020). Structure, Function, and Antigenicity of the SARS-CoV-2 Spike Glycoprotein.
1416 Cell *181*, 281-292 e286.
1417 Wang, C., Li, W., Drabek, D., Okba, N.M.A., van Haperen, R., Osterhaus, A., van
1418 Kuppeveld, F.J.M., Haagmans, B.L., Grosveld, F., and Bosch, B.J. (2020). A human
1419 monoclonal antibody blocking SARS-CoV-2 infection. Nat Commun *11*, 2251.
1420 Winkler, E.S., Gilchuk, P., Yu, J., Bailey, A.L., Chen, R.E., Chong, Z., Zost, S.J., Jang,
1421 H., Huang, Y., Allen, J.D., *et al.* (2021). Human neutralizing antibodies against SARS-
1422 CoV-2 require intact Fc effector functions for optimal therapeutic protection. Cell *184*,
1423 1804-1820 e1816.
1424 Worldometer (2021). COVID-19 CORONAVIRUS PANDEMIC.
1425 Wrapp, D., De Vlieger, D., Corbett, K.S., Torres, G.M., Wang, N., Van Breedam, W.,
1426 Roose, K., van Schie, L., Team, V.-C.C.-R., Hoffmann, M., *et al.* (2020a). Structural
1427 Basis for Potent Neutralization of Betacoronaviruses by Single-Domain Camelid
1428 Antibodies. Cell *181*, 1004-1015 e1015.
1429 Wrapp, D., Wang, N., Corbett, K.S., Goldsmith, J.A., Hsieh, C.L., Abiona, O., Graham,
1430 B.S., and McLellan, J.S. (2020b). Cryo-EM structure of the 2019-nCoV spike in the
1431 prefusion conformation. Science *367*, 1260-1263.
1432 Wu, F., Liu, M., Wang, A., Lu, L., Wang, Q., Gu, C., Chen, J., Wu, Y., Xia, S., Ling, Y.,
1433 *et al.* (2020a). Evaluating the Association of Clinical Characteristics With Neutralizing
1434 Antibody Levels in Patients Who Have Recovered From Mild COVID-19 in Shanghai,
1435 China. JAMA Intern Med *180*, 1356-1362.
1436 Wu, F., Zhao, S., Yu, B., Chen, Y.M., Wang, W., Song, Z.G., Hu, Y., Tao, Z.W., Tian,
1437 J.H., Pei, Y.Y., *et al.* (2020b). A new coronavirus associated with human respiratory
1438 disease in China. Nature *579*, 265-269.
1439 Wu, Y., Wang, F., Shen, C., Peng, W., Li, D., Zhao, C., Li, Z., Li, S., Bi, Y., Yang, Y., *et*
1440 *al.* (2020c). A noncompeting pair of human neutralizing antibodies block COVID-19
1441 virus binding to its receptor ACE2. Science *368*, 1274-1278.
1442 Xie, X., Muruato, A., Lokugamage, K.G., Narayanan, K., Zhang, X., Zou, J., Liu, J.,
1443 Schindewolf, C., Bopp, N.E., Aguilar, P.V., *et al.* (2020a). An Infectious cDNA Clone of
1444 SARS-CoV-2. Cell Host Microbe *27*, 841-848 e843.
1445 Xie, X., Muruato, A.E., Zhang, X., Lokugamage, K.G., Fontes-Garfias, C.R., Zou, J.,
1446 Liu, J., Ren, P., Balakrishnan, M., Cihlar, T., *et al.* (2020b). A nanoluciferase SARS-
1447 CoV-2 for rapid neutralization testing and screening of anti-infective drugs for COVID-
1448 19. Nat Commun *11*, 5214.

1449 Yuan, M., Wu, N.C., Zhu, X., Lee, C.D., So, R.T.Y., Lv, H., Mok, C.K.P., and Wilson,
1450 I.A. (2020). A highly conserved cryptic epitope in the receptor binding domains of
1451 SARS-CoV-2 and SARS-CoV. Science *368*, 630-633.
1452 Zaki, A.M., van Boheemen, S., Bestebroer, T.M., Osterhaus, A.D., and Fouchier, R.A.
1453 (2012). Isolation of a novel coronavirus from a man with pneumonia in Saudi Arabia. N
1454 Engl J Med *367*, 1814-1820.
1455 Zhu, N., Zhang, D., Wang, W., Li, X., Yang, B., Song, J., Zhao, X., Huang, B., Shi, W.,
1456 Lu, R.*, et al.* (2020). A Novel Coronavirus from Patients with Pneumonia in China, 2019.
1457 N Engl J Med *382*, 727-733.
1458 Zivanov, J., Nakane, T., Forsberg, B.O., Kimanius, D., Hagen, W.J., Lindahl, E., and
1459 Scheres, S.H. (2018). New tools for automated high-resolution cryo-EM structure
1460 determination in RELION-3. Elife *7*.
1461 Zohar, T., Loos, C., Fischinger, S., Atyeo, C., Wang, C., Slein, M.D., Burke, J., Yu, J.,
1462 Feldman, J., Hauser, B.M.*, et al.* (2020). Compromised Humoral Functional Evolution
1463 Tracks with SARS-CoV-2 Mortality. Cell *183*, 1508-1519 e1512.
1464 The PyMOL Molecular Graphics System, Version 1.2r3pre, Schrödinger, LLC
1465

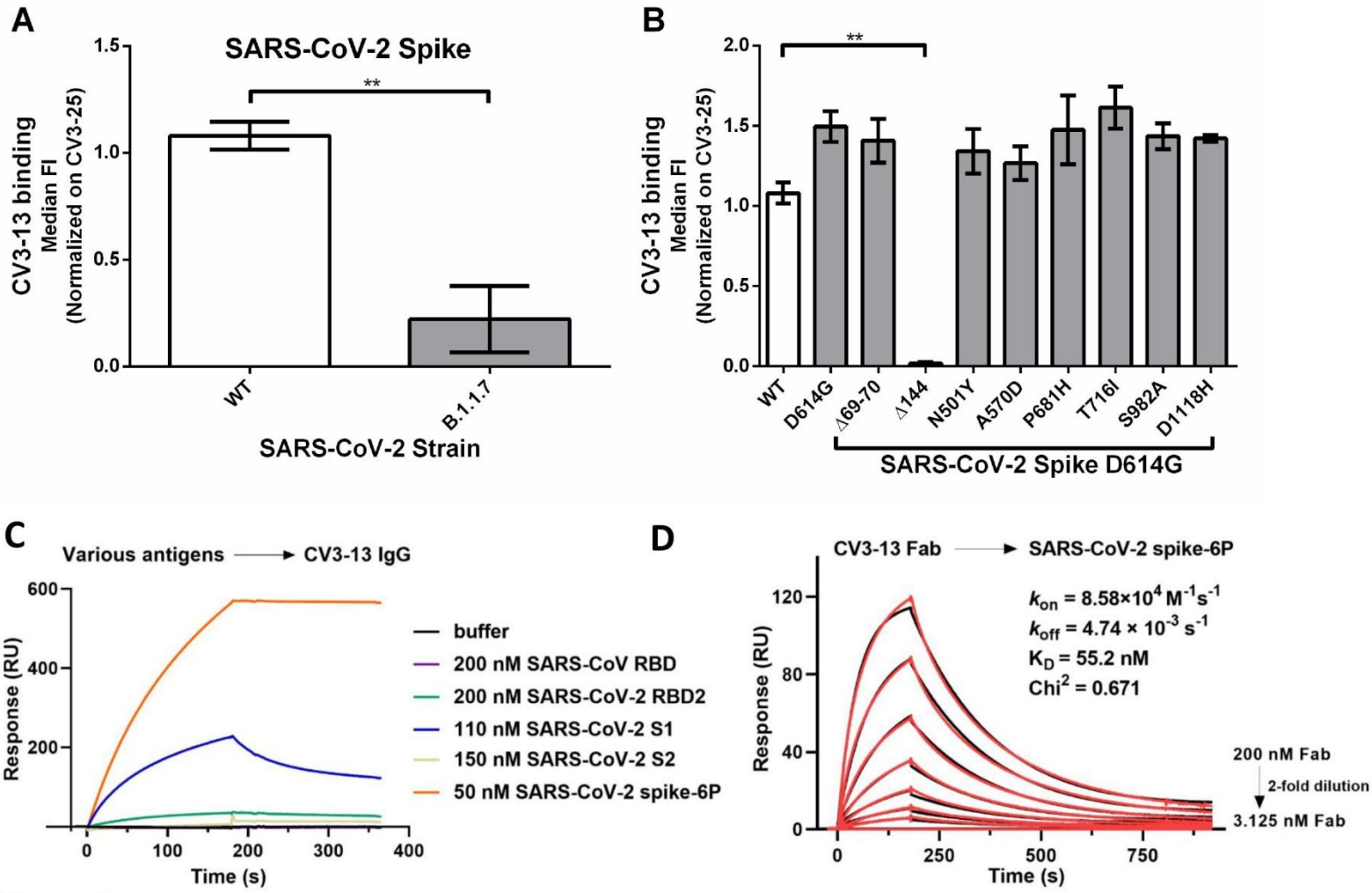

Figure 1

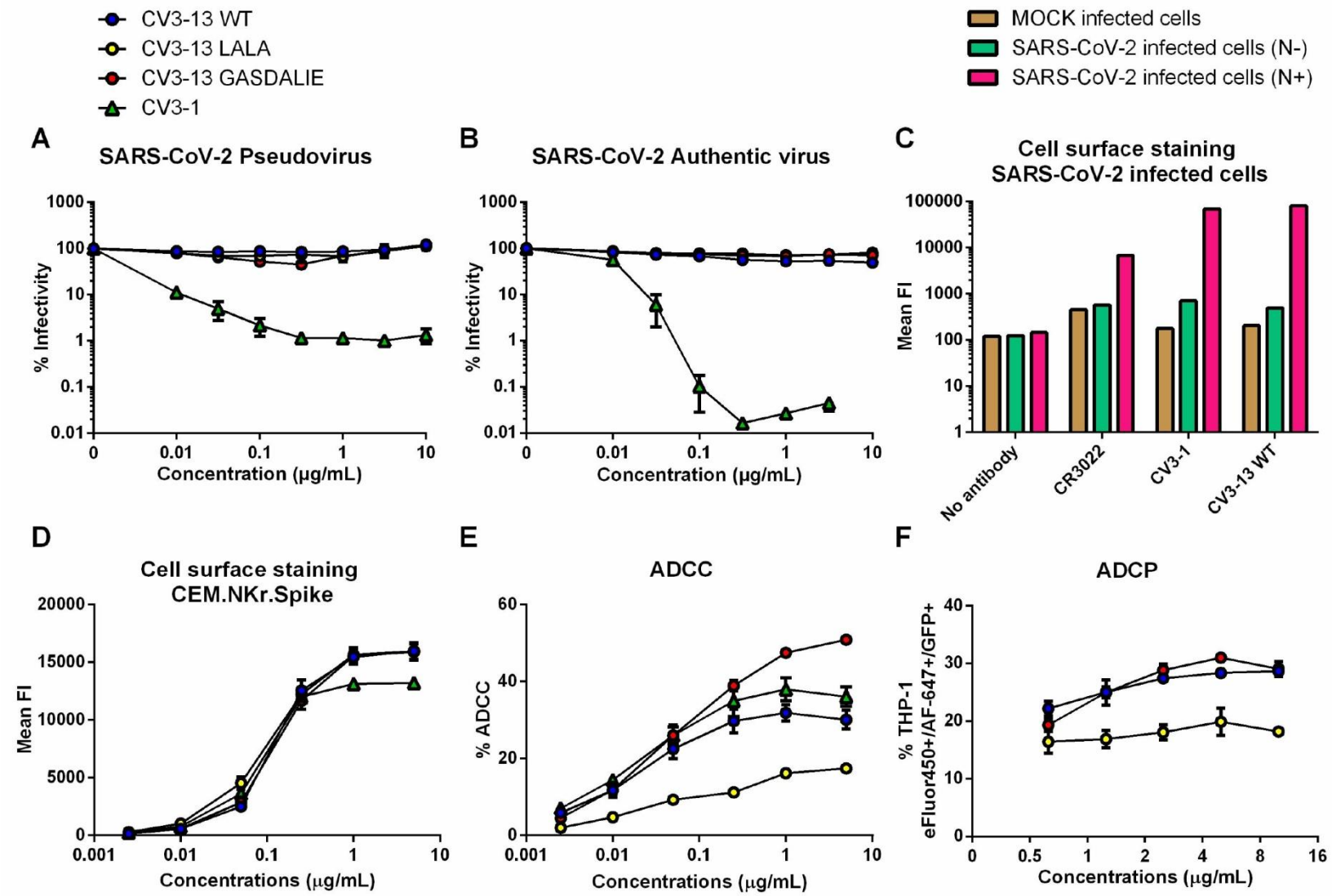

Figure 2

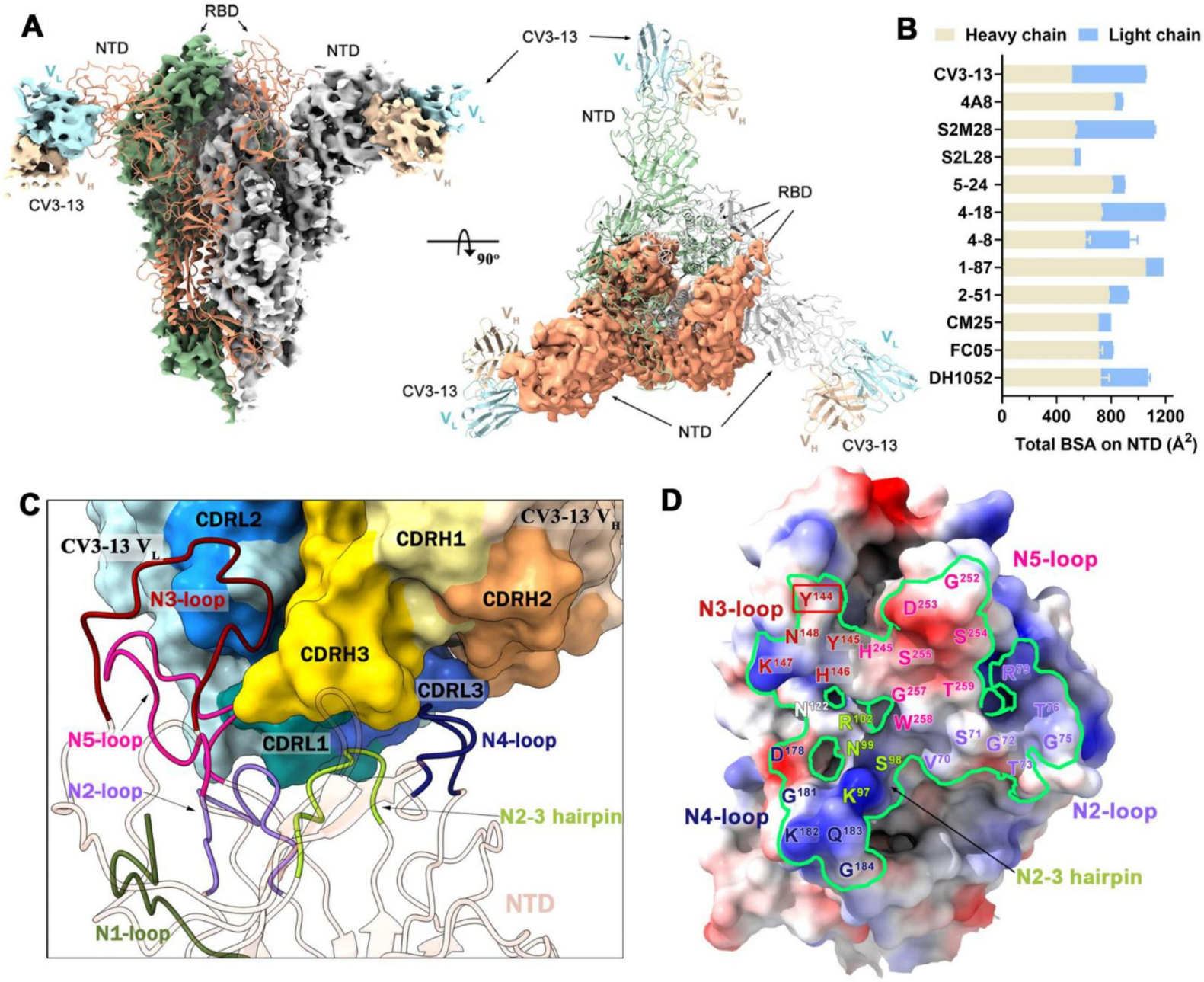

Figure 3

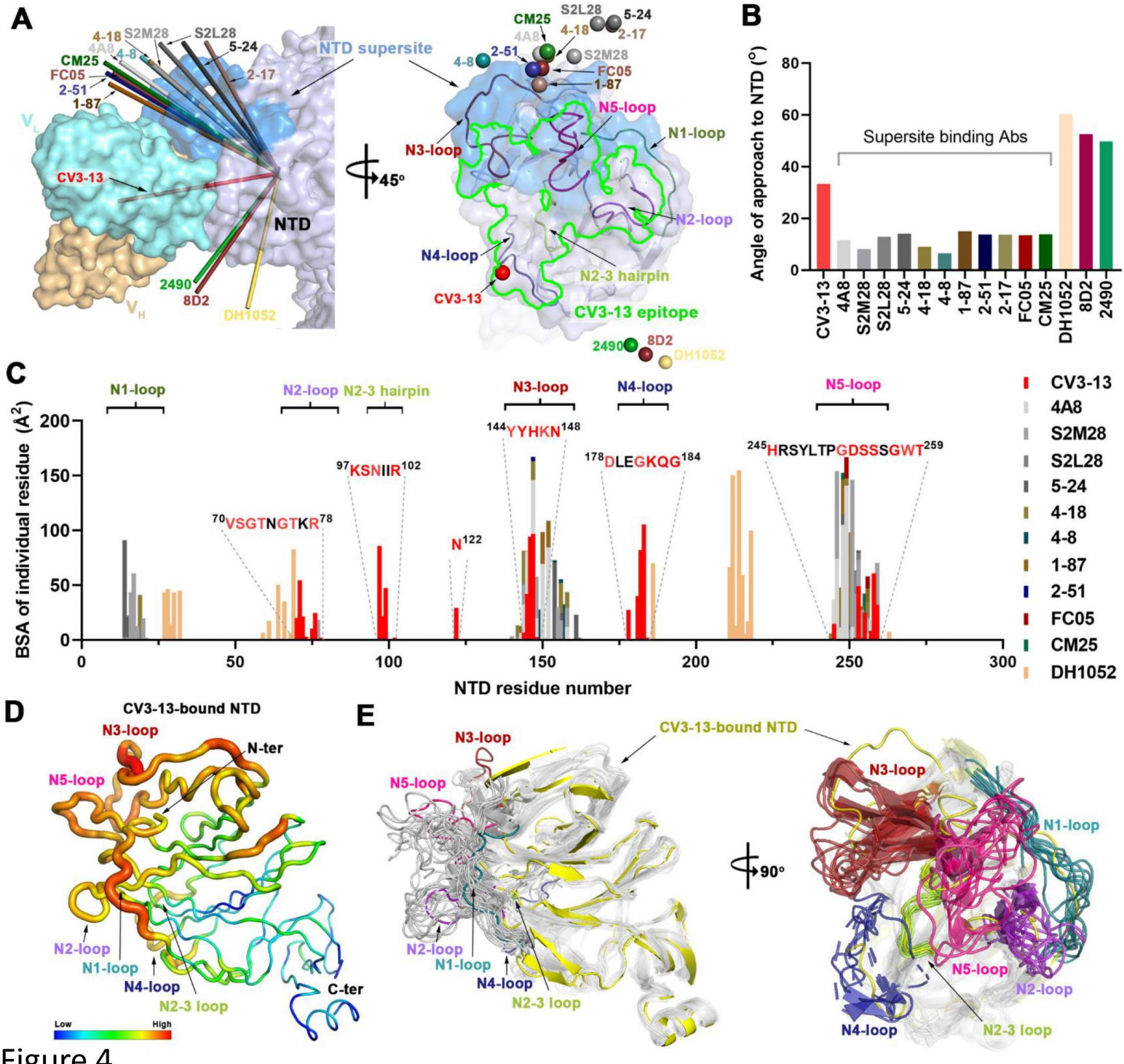

Figure 4

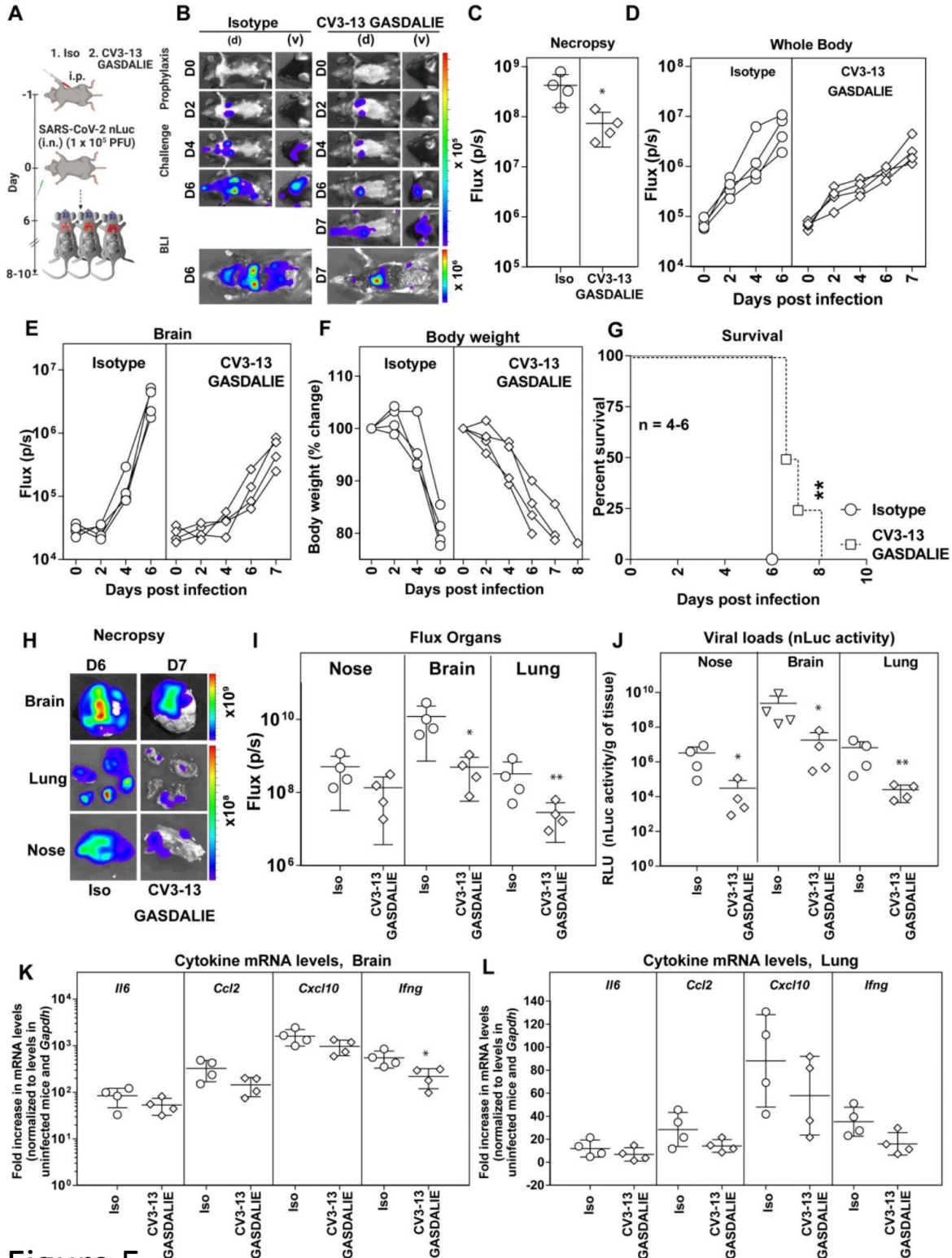

Figure 5

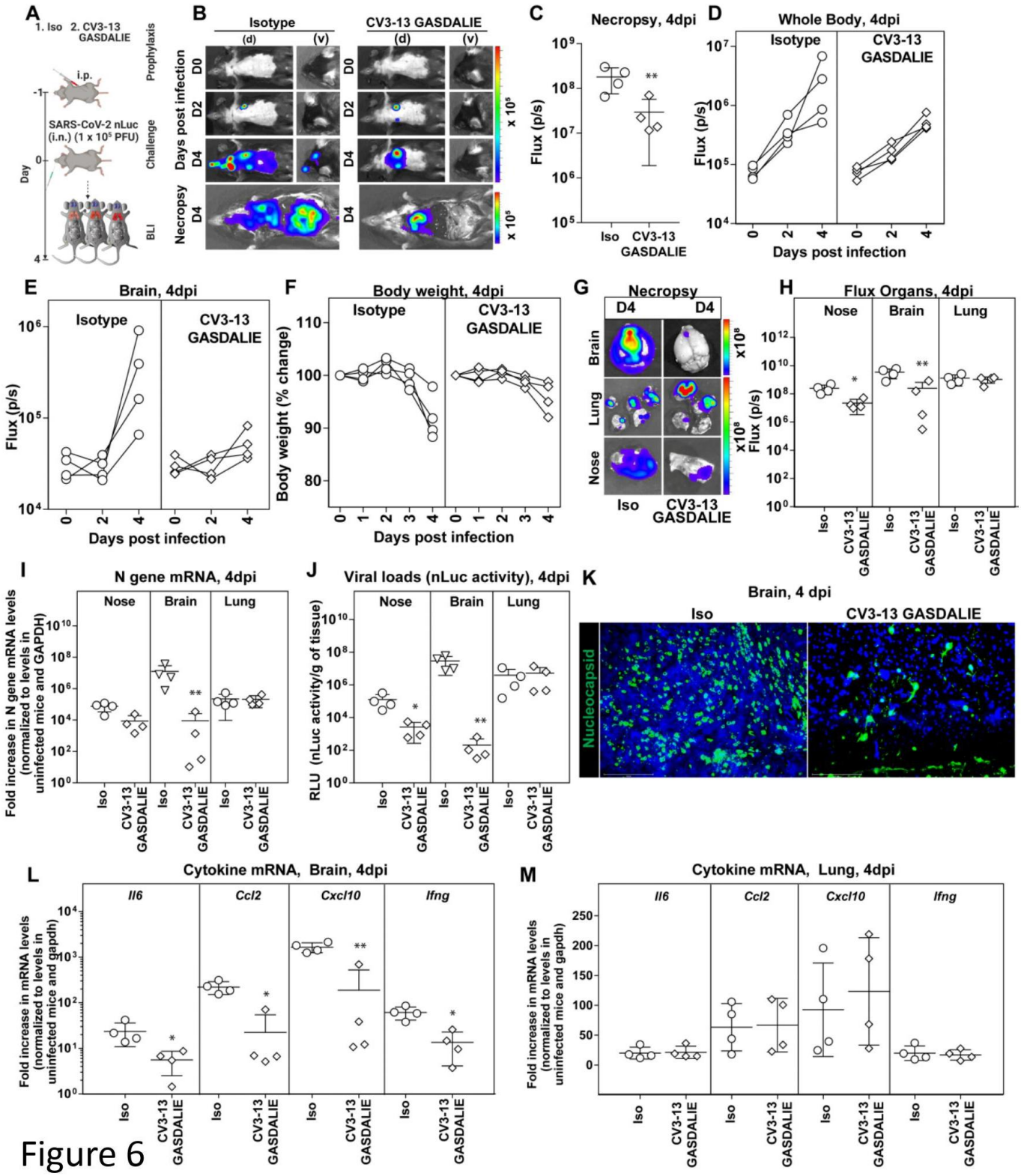

Figure 6

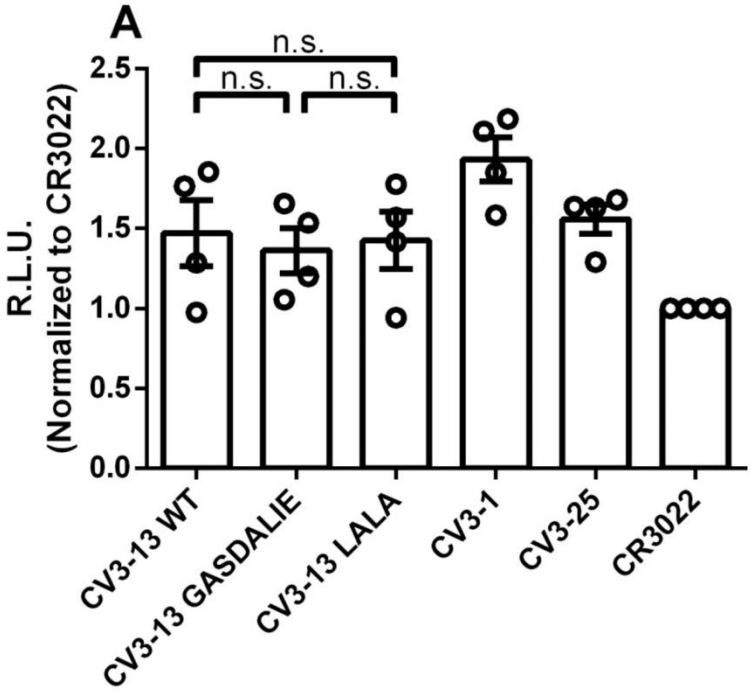

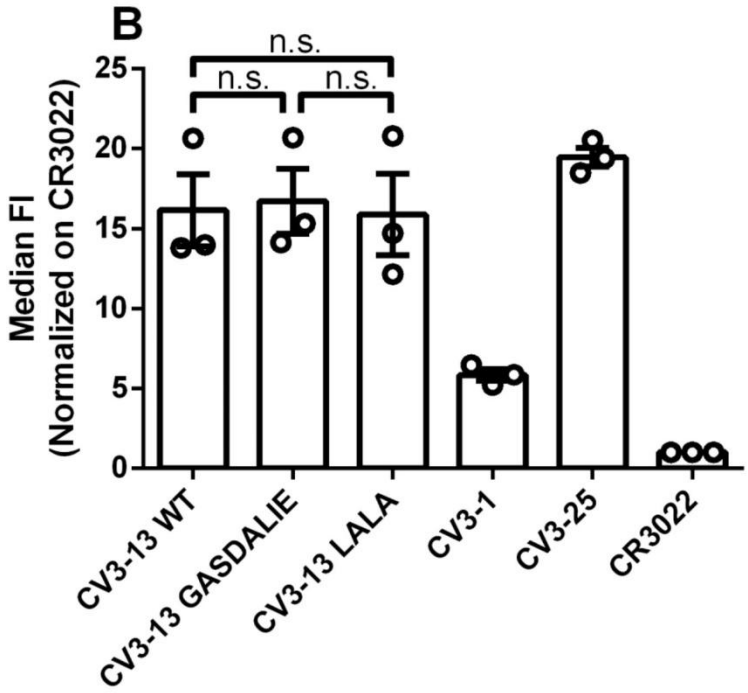

Supplemental Figure 1

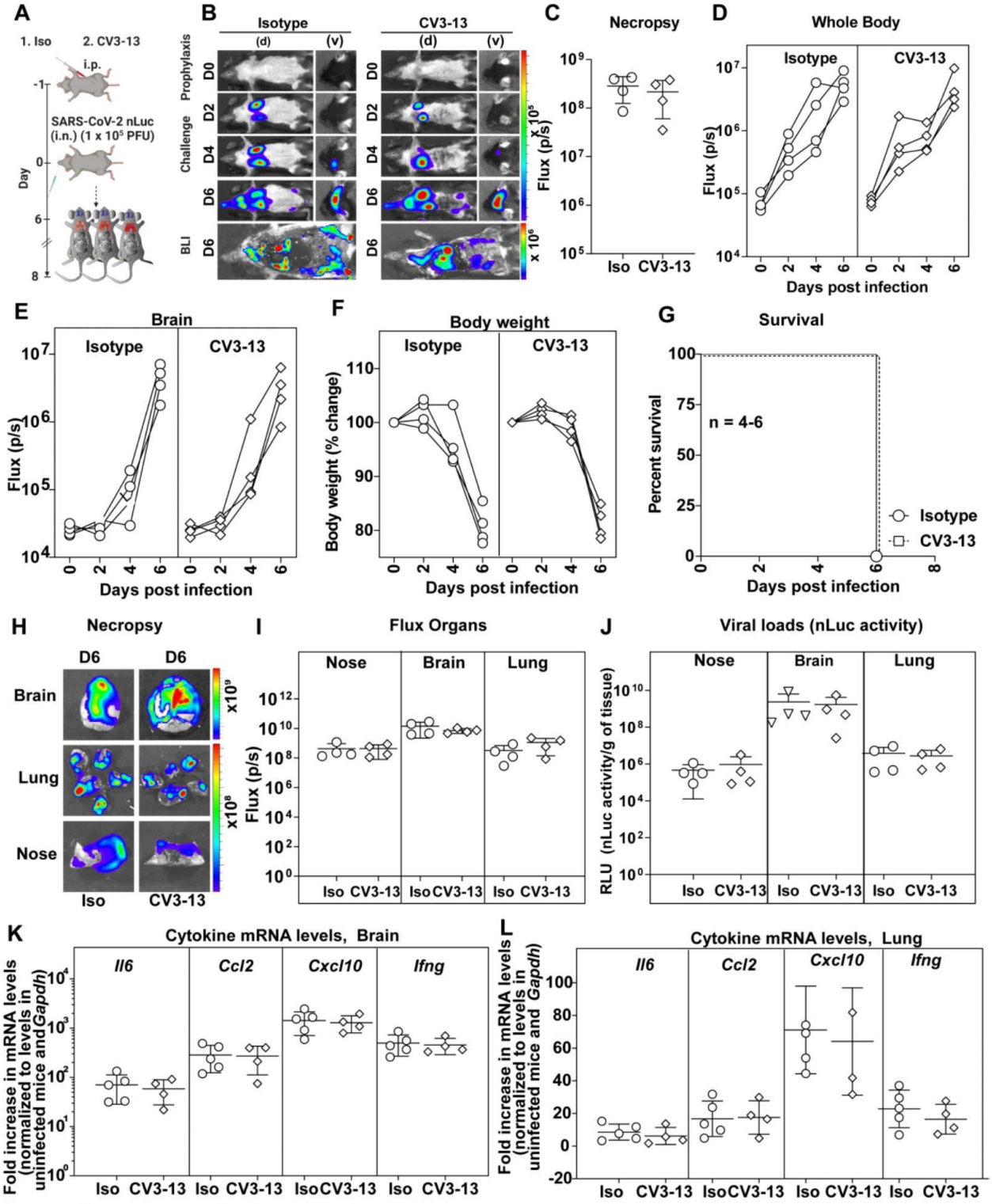

Supplemental Figure 2

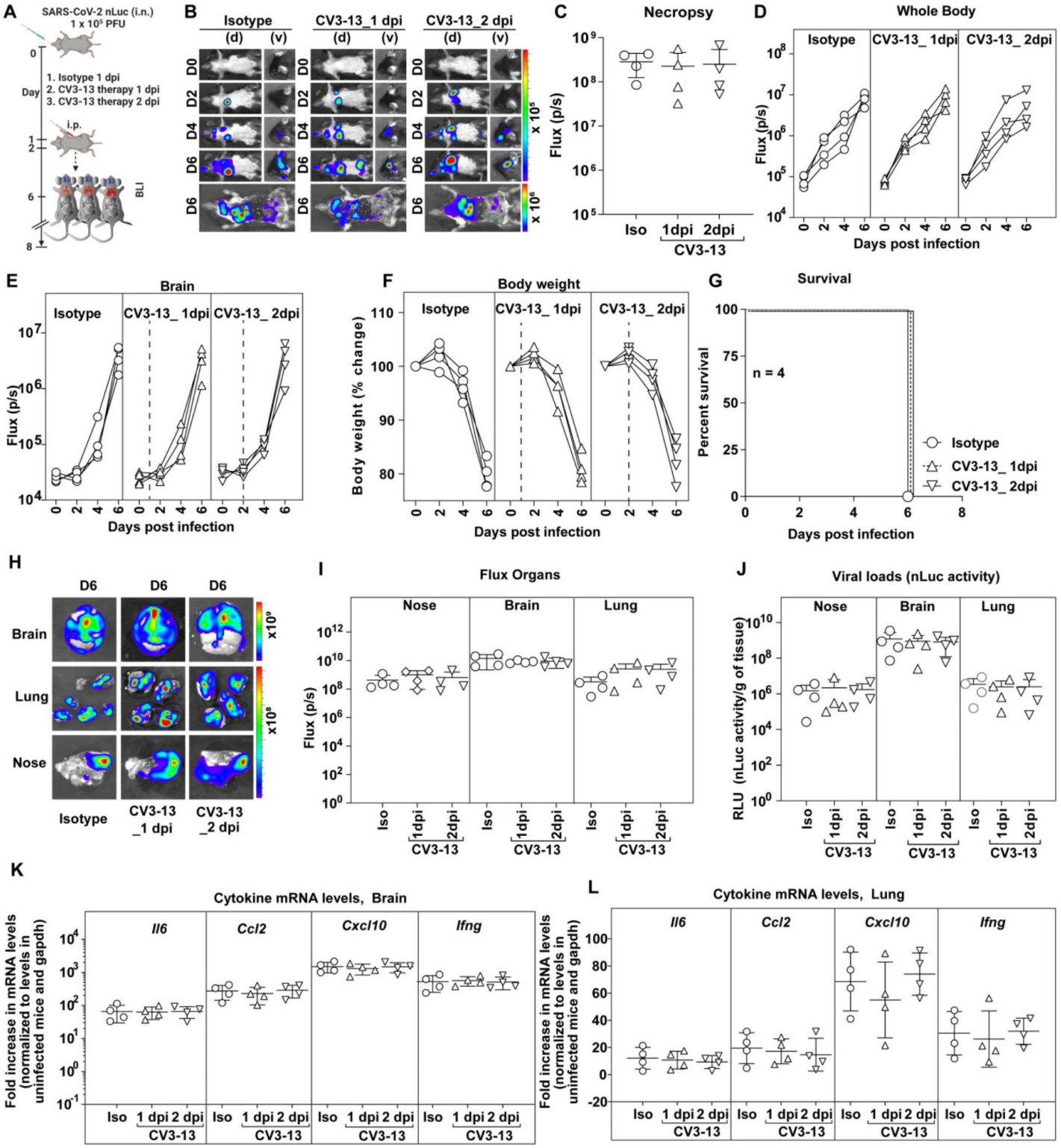

Supplemental Figure 3

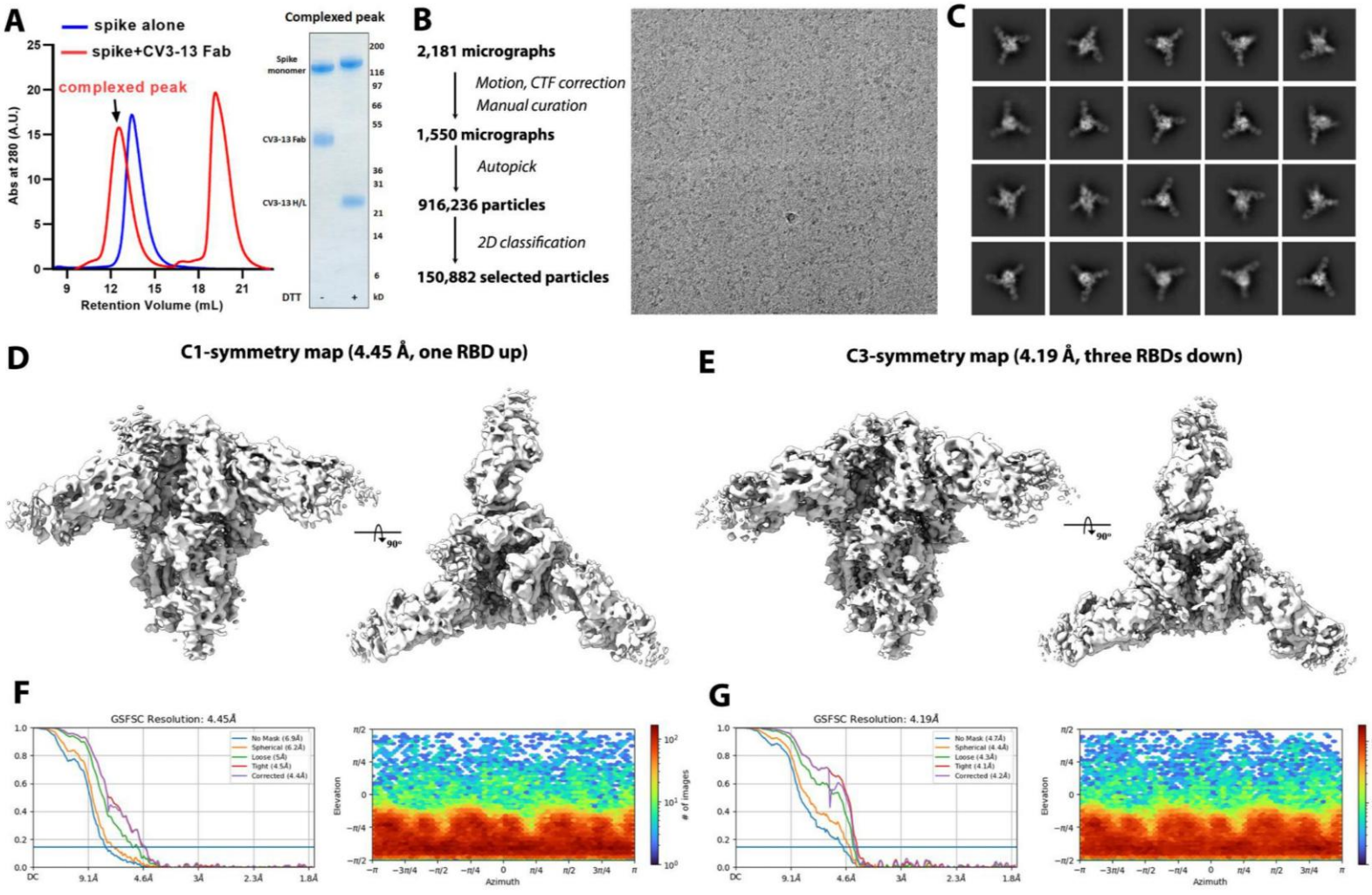

Supplemental Figure 4

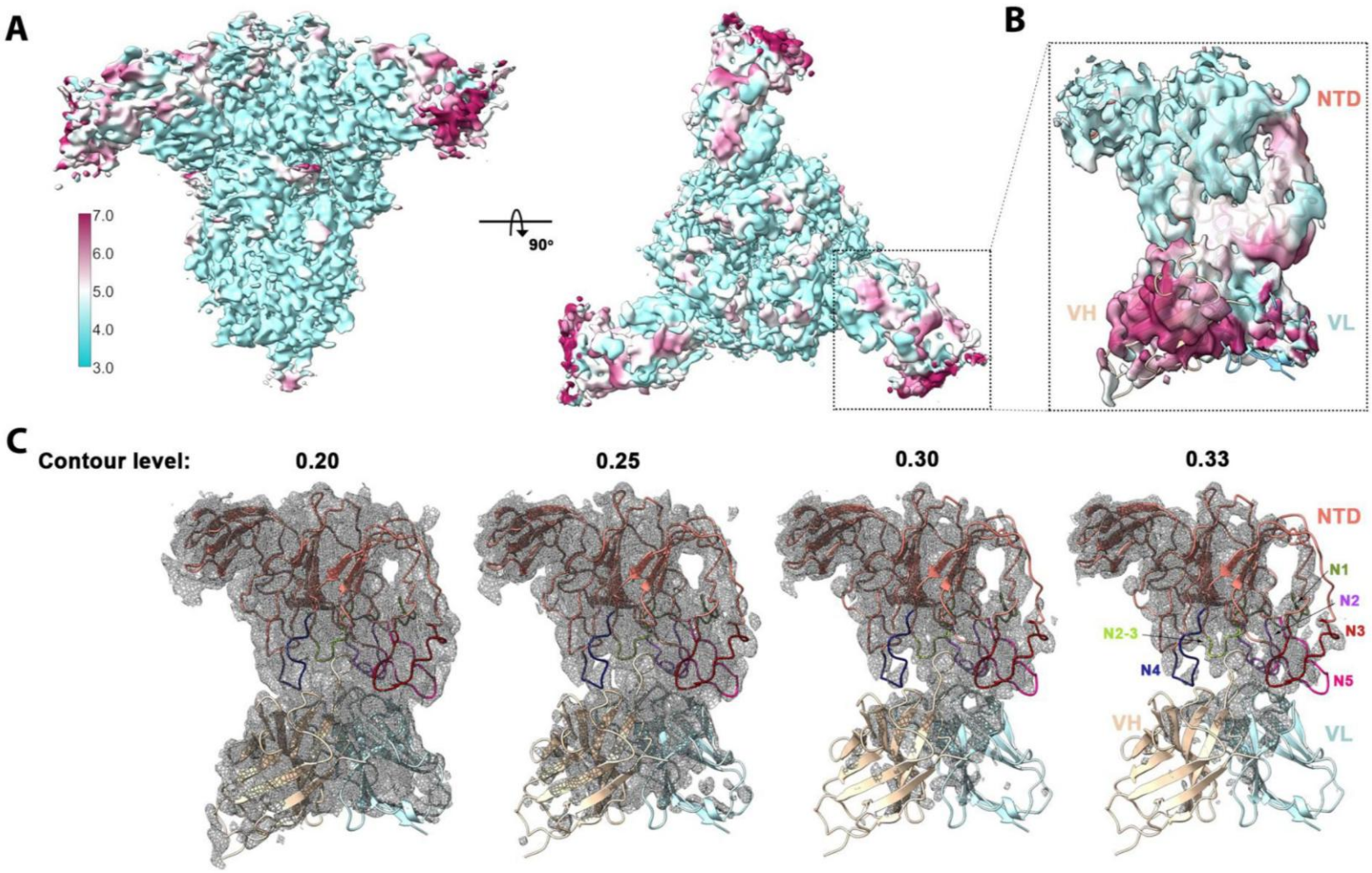

Supplemental Figure 5

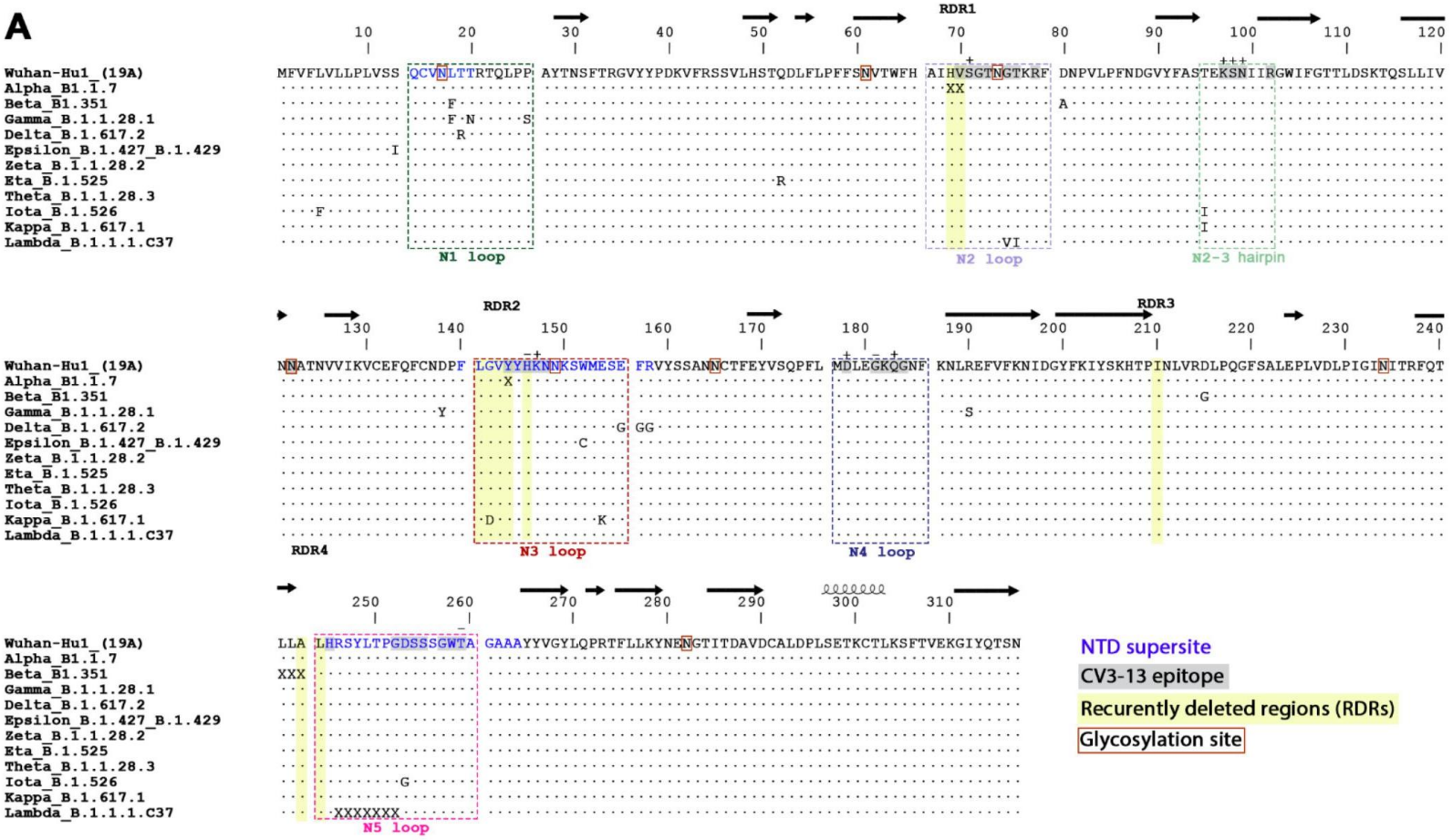

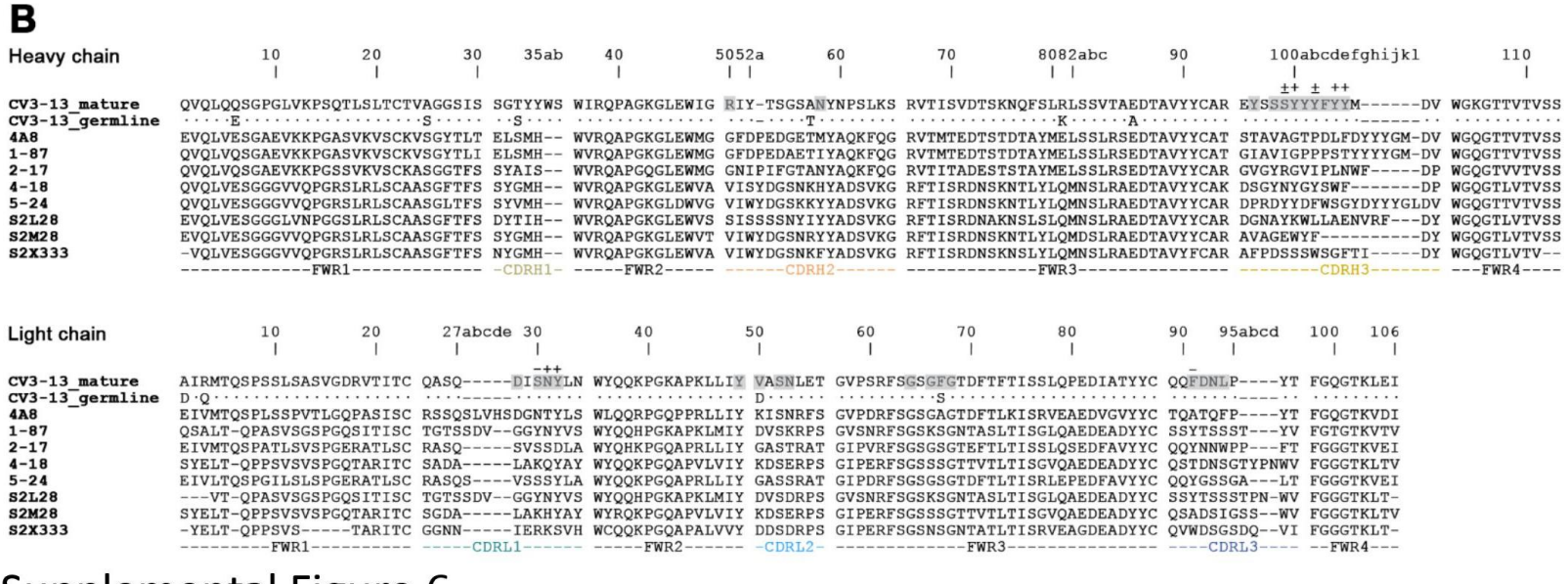

Supplemental Figure 6